Volume 25
Number 2
14 January 2023
Pages 881–1374

PCCP

Physical Chemistry Chemical Physics

rsc.li/pccp

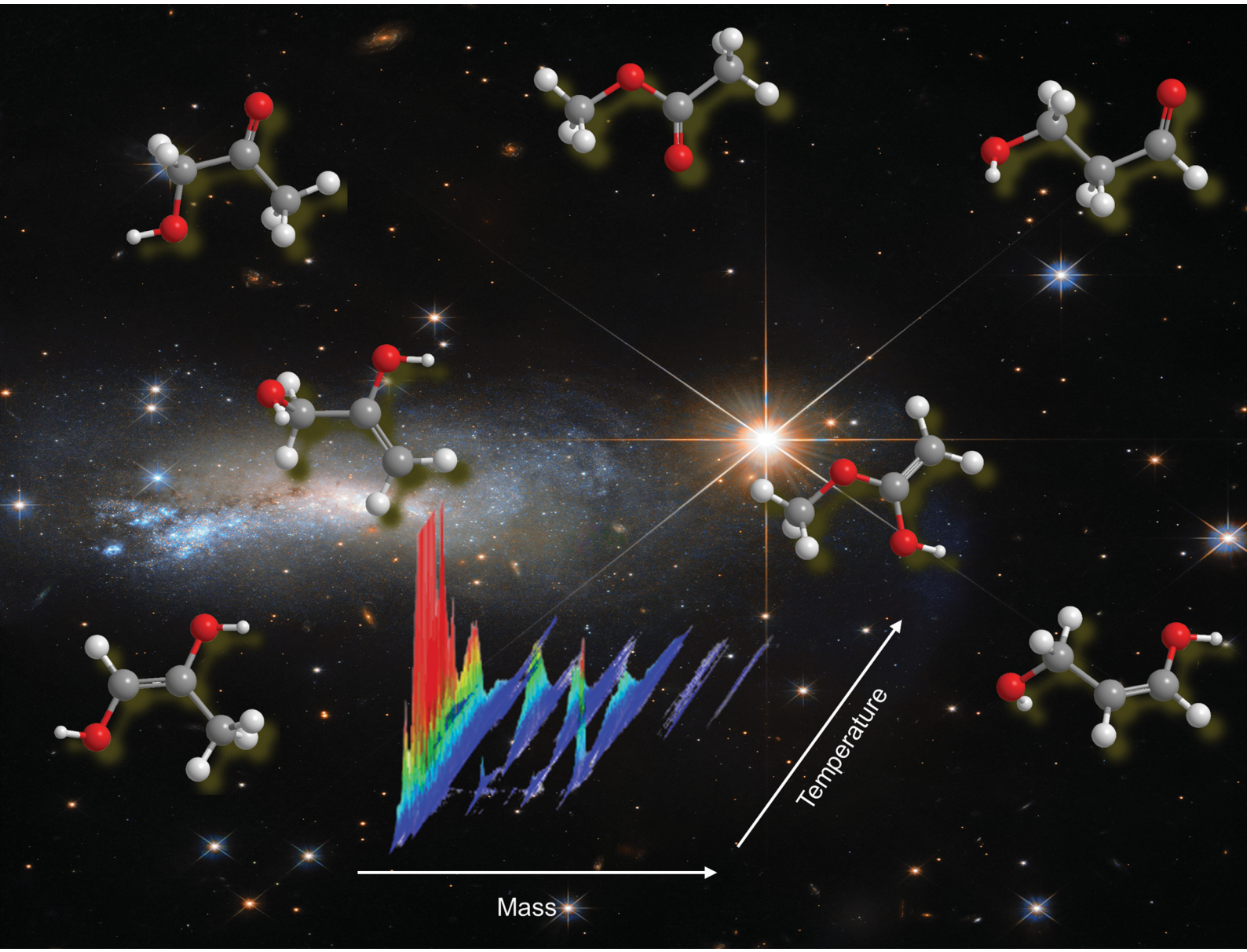

ISSN 1463-9076

PAPER

Ralf I. Kaiser *et al.*

Mechanistical study on the formation of hydroxyacetone (CH_3COCH_2OH), methyl acetate (CH_3COOCH_3), and 3-hydroxypropanal ($HCOCH_2CH_2OH$) along with their enol tautomers (prop-1-ene-1,2-diol ($CH_3C(OH)CHOH$), prop-2-ene-1,2-diol ($CH_2C(OH)CH_2OH$), 1-methoxyethen-1-ol ($CH_3OC(OH)CH_2$) and prop-1-ene-1,3-diol ($HOCH_2CHCHOH$)) in interstellar ice analogs

ROYAL SOCIETY OF CHEMISTRY

PCCP

ROYAL SOCIETY OF CHEMISTRY

PAPER

Cite this: *Phys. Chem. Chem. Phys.*, 2023, **25**, 936

Mechanistical study on the formation of hydroxyacetone (CH_3COCH_2OH), methyl acetate (CH_3COOCH_3), and 3-hydroxypropanal ($HCOCH_2CH_2OH$) along with their enol tautomers (prop-1-ene-1,2-diol ($CH_3C(OH)CHOH$), prop-2-ene-1,2-diol ($CH_2C(OH)CH_2OH$), 1-methoxyethen-1-ol ($CH_3OC(OH)CH_2$) and prop-1-ene-1,3-diol ($HOCH_2CHCHOH$)) in interstellar ice analogs†

Jia Wang, [ab] Joshua H. Marks, [ab] Andrew M. Turner, [ab] Anatoliy A. Nikolayev, [cd] Valeriy Azyazov, [c] Alexander M. Mebel [e] and Ralf I. Kaiser *[ab]

We unravel, for the very first time, the formation pathways of hydroxyacetone (CH_3COCH_2OH), methyl acetate (CH_3COOCH_3), and 3-hydroxypropanal ($HCOCH_2CH_2OH$), as well as their enol tautomers within mixed ices of methanol (CH_3OH) and acetaldehyde (CH_3CHO) analogous to interstellar ices in the ISM exposed to ionizing radiation at ultralow temperatures of 5 K. Exploiting photoionization reflectron time-of-flight mass spectrometry (PI-ReToF-MS) and isotopically labeled ices, the reaction products were selectively photoionized allowing for isomer discrimination during the temperature-programmed desorption phase. Based on the distinct mass-to-charge ratios and ionization energies of the identified species, we reveal the formation pathways of hydroxyacetone (CH_3COCH_2OH), methyl acetate (CH_3COOCH_3), and 3-hydroxypropanal ($HCOCH_2CH_2OH$) *via* radical–radical recombination reactions and of their enol tautomers (prop-1-ene-1,2-diol ($CH_3C(OH)CHOH$), prop-2-ene-1,2-diol ($CH_2C(OH)CH_2OH$), 1-methoxyethen-1-ol ($CH_3OC(OH)CH_2$) and prop-1-ene-1,3-diol ($HOCH_2CHCHOH$)) *via* keto-enol tautomerization. To the best of our knowledge, 1-methoxyethen-1-ol ($CH_3OC(OH)CH_2$) and prop-1-ene-1,3-diol ($HOCH_2CHCHOH$) are experimentally identified for the first time. Our findings help to constrain the formation mechanism of hydroxyacetone and methyl acetate detected within star-forming regions and suggest that the hitherto astronomically unobserved isomer 3-hydroxypropanal and its enol tautomers represent promising candidates for future astronomical searches. These enol tautomers may contribute to the molecular synthesis of biologically relevant molecules in deep space due to their nucleophilic character and high reactivity.

Received 2nd August 2022,
Accepted 14th October 2022

DOI: 10.1039/d2cp03543j

rsc.li/pccp

1. Introduction

Complex organic molecules (COMs) – per astronomical definition, organic molecules containing six or more atoms of carbon, hydrogen, oxygen, and nitrogen, such as aldehydes (HCOR) [1], ketones (RCOR′) [2], carboxylic acids (RCOOH) [3], esters (RCOOR′) [4], and amides ($RCONH_2$) [5], with R and R′ being organic groups – are omnipresent in the interstellar medium (ISM) (Fig. 1).[1,2] Understanding the abiotic formation pathways of these key classes of COMs is of fundamental importance to the

[a] *W. M. Keck Research Laboratory in Astrochemistry, University of Hawaii at Manoa, Honolulu, HI 96822, USA. E-mail: ralfk@hawaii.edu*
[b] *Department of Chemistry, University of Hawaii at Manoa, Honolulu, HI 96822, USA*
[c] *Lebedev Physical Institute, Samara 443011, Russia*
[d] *Samara National Research University, Samara 443086, Russia*
[e] *Department of Chemistry and Biochemistry, Florida International University, Miami, Florida 33199, USA*

† Electronic supplementary information (ESI) available. See DOI: https://doi.org/10.1039/d2cp03543j

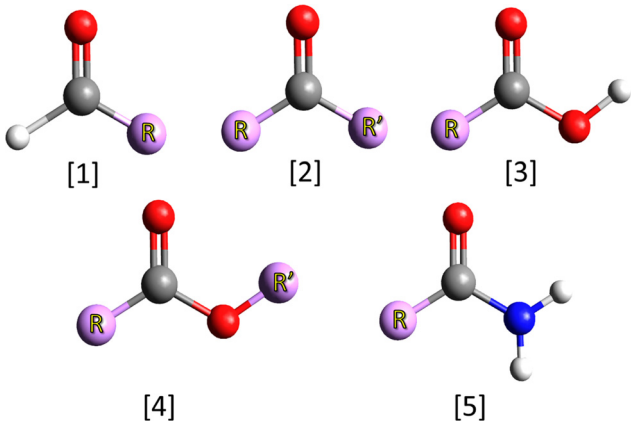

Fig. 1 Five classes of COMs observed in cold molecular clouds and star forming regions: aldehydes (HCOR) [1], ketones (RCOR′) [2], carboxylic acids (RCOOH) [3], esters (RCOOR′) [4], and amides ($RCONH_2$) [5]; R and R′ represent organic groups.

laboratory astrophysics and astronomy communities to unravel key reaction pathways to complex organics of astrobiological importance such as amino acids,[3–8] dipeptides,[8] (poly)alcohols[9–16] and glycerol phosphates.[17] These molecules represent molecular building blocks of, *e.g.*, polypeptides, enzymes, nucleobases, and cell membranes.[18,19] A fundamental knowledge of the formation of structural isomers–molecules with the same molecular formula, but of distinct atomic connectivities – of COMs is of critical significance since these molecules are recognized as tracers of physical and chemical conditions of interstellar environments and as testbeds to validate chemical models of molecular clouds and star-forming regions through astrochemical modeling.[20] However, despite the key role of structural isomers as tracers to define the evolutionary stage of molecular clouds and star-forming regions along with their physical and chemical boundary conditions, there is still incomplete understanding of the underlying formation mechanisms, with astrochemical models of *gas-phase-only-chemistry* yielding a factor of up to 1000 less of complex organics such as methanol (CH_3OH) than observed astronomically.[21–24] A crucial point of concern is that the majority of astrochemical models have been postulating that the ice mantle is chemically inert and that only the ice surface takes part in the synthesis of new molecules despite the fact that interaction of ionizing radiation within ices leads to the formation of COMs[2,22] and that surface layers contribute less than 1% to the mass of the condensed molecules on these grains.

Very recently, special attention has been devoted to distinct $C_3H_6O_2$ isomers hydroxyacetone (CH_3COCH_2OH, **1**), methyl acetate (CH_3COOCH_3, **2**), 3-hydroxypropanal ($HCOCH_2CH_2OH$, **3**), and 2-methoxyacetaldehyde ($HCOCH_2OCH_3$, **4**) (Fig. 2a). Hydroxyacetone (CH_3COCH_2OH, **1**) was first identified by Zhou *et al.* (2020) with the Atacama Large Millimeter Array (ALMA) toward a young solar-type protostar IRAS 16293–2422B. Based on the local thermodynamic equilibrium analysis, the rotational temperature and column density of hydroxyacetone (CH_3COCH_2OH, **1**) were derived to be 160 ± 21 K and (1.2 ± 1.0) × 10^{16} cm^{-2}, respectively.[25] The detection of methyl acetate (CH_3COOCH_3, **2**) was first accomplished by Tercero *et al.* through IRAM 30 m observations of Orion Nebula.[26] 215 unblended transitions between 80 and 281 GHz were assigned based on the laboratory work.[27] A rotational temperature of 150 ± 20 K and a total column density of (4.2 ± 0.5) × 10^{15} cm^{-2} were extracted, too.[26] We note that two searches for hydroxyacetone (CH_3COCH_2OH, **1**) toward Sagittarius B2(N) were carried out using both the Caltech Submillimeter Observatory (CSO) and the Arizona Radio Observatory (ARO) 12 m telescope;[28,29] however, the detection is inconclusive to be defined as 'firm'.[28] Until now, hydroxyacetone (CH_3COCH_2OH, **1**) and methyl acetate (CH_3COOCH_3, **2**) have not been reported toward the same source.

Methyl acetate (CH_3COOCH_3, **2**) represents the simplest ester of acetic acid (CH_3COOH) in which the hydrogen atom of the carboxylic acid moiety (COOH) is replaced by a methyl (CH_3) group. The bifunctional hydroxyacetone (CH_3COCH_2OH, **1**) carries two functional groups: a carbonyl moiety (C═O) and a hydroxyl group (OH). It exemplifies a methyl-substituted glycolaldehyde ($HCOCH_2OH$) derivative and is linked to the 3C sugar dihydroxyacetone ($HOCH_2COCH_2OH$, '$C_3(H_2O)_3$'), a compound widely observed in the soluble organic fraction of carbonaceous chondrites,[29] by replacing a hydrogen atom of the methyl group by a second hydroxyl group.[25] In organic chemistry, hydroxyacetone (CH_3COCH_2OH, **1**) has been discussed as a critical starting material in the synthesis of aldehydes and ketones (Fig. 1).[25,28] Therefore, understanding the production pathways to hydroxyacetone (CH_3COCH_2OH, **1**) and methyl acetate (CH_3COOCH_3, **2**) may help in answering the question of the origin and evolution of fundamental precursors to biorelevant molecules connected to the origins of life in the universe on the molecular level.[25,30]

Various synthetic routes have been proposed for the formation mechanisms of hydroxyacetone (CH_3COCH_2OH, **1**) and methyl acetate (CH_3COOCH_3, **2**). These involve gas-phase ion–molecule reactions as well as reactions on the surface of interstellar grains. First, Story *et al.* proposed a pathway for the formation of hydroxyacetone (CH_3COCH_2OH, **1**) in the gas phase (reaction (1)) through $(CH_3)_2COO$ Criegee intermediates:[31]

$$(CH_3)_2COO \rightarrow CH_2{=}C(CH_3)OOH \rightarrow CH_3COCH_2OH \quad (1)$$

A reaction barrier of 97 kJ mol^{-1} relative to the Criegee intermediate $(CH_3)_2COO$ reactant was calculated for the OH transfer from CH_2═$C(CH_3)OOH$ at the B3LYP/6-31G(d,p) level of theory.[32] Hydroxyacetone (CH_3COCH_2OH, **1**) is postulated to be prepared *via* reaction (2):[25]

$$CH_3COOH_2^+ + CH_3OH \rightarrow CH_3COCH_2OH_2^+ + H_2O \quad (2a)$$

$$CH_3COCH_2OH_2^+ + e^- \rightarrow CH_3COCH_2OH + H \quad (2b)$$

or *via* the radical–radical recombination (reaction (3)) of $\dot{C}H_2OH$ and $CH_3\dot{C}O$:[33]

$$\dot{C}H_2OH + CH_3\dot{C}O \rightarrow CH_3COCH_2OH \quad (3)$$

As for the reaction routes synthesizing methyl acetate (CH_3COOCH_3, **2**) in the gas phase, Das *et al.* proposed reactions (4) and (5):[33]

$$C_3H_7O_2^+ + e^- \rightarrow CH_3COOCH_3 + H \quad (4)$$

$$CH_3\dot{O} + CH_3\dot{C}O \rightarrow CH_3COOCH_3 \quad (5)$$

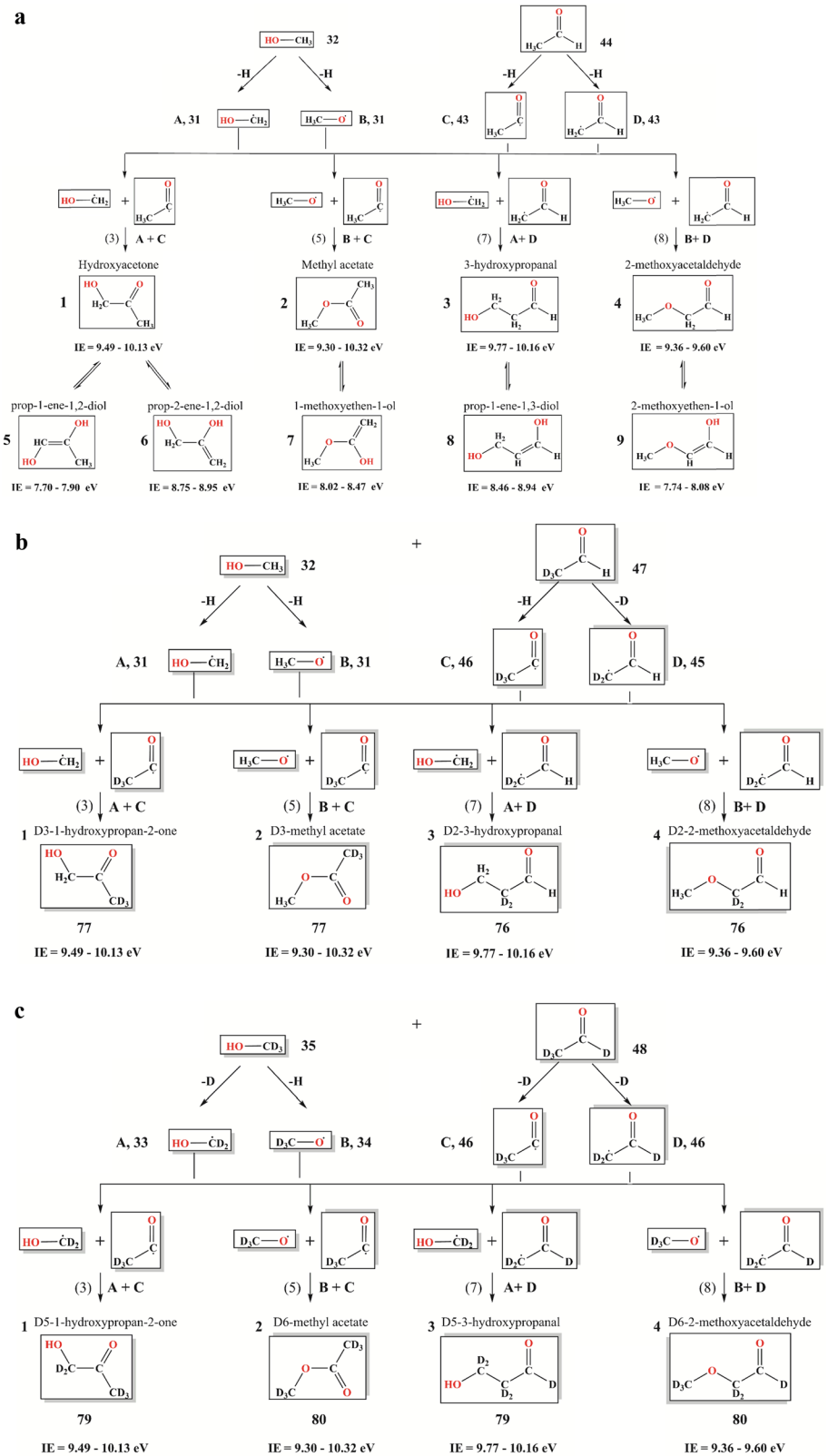

Fig. 2 (a). Proposed formation pathways of the four $C_3H_6O_2$ isomers (m/z = 74) in CH_3OH:CH_3CHO ice after electron irradiation. The adiabatic ionization energies are computed at the CCSD(T)-F12/CC-pVTZ-F12//ωB97XD/cc-pVTZ level of theory including zero-point vibrational energies and are corrected by incorporating the error analysis (Table S1, ESI†). (b). Proposed formation pathways of isomers **1–4** at m/z = 77 (**1** and **2**) and at m/z = 76 (**3** and **4**) *via* radical–radical reactions in deuterated CH_3OH–CD_3CHO ice after low-dose electron irradiation. (c). Proposed formation pathways of the isomers **1–4** at m/z = 79 (**1** and **3**) and at m/z = 80 (**2** and **4**) *via* radical–radical reactions in CD_3OH–CD_3CDO ice after low-dose electron irradiation.

Needless to say, the ion-molecule reactions (2) and (4) have neither been studied in the laboratory nor computationally and hence must be regarded as speculative. Further, three-body reactions such as (3) and (5) do not happen in molecular clouds due to the low number densities.[22] Hence, reactions (3) and (5) are without merit and cannot lead to methyl acetate (CH_3COOCH_3, **2**) or hydroxyacetone (CH_3COCH_2OH, **1**) in the gas phase.

Second, on icy grains, one reaction route synthesizing methyl acetate (CH_3COOCH_3, **2**) might be the carbonylation reaction (reaction (6)) of dimethyl ether (CH_3OCH_3) and carbon monoxide (CO).[34] However, a one-step insertion into the C–O bond has a barrier higher than 100 kJ mol^{-1} and hence cannot operate at the 10 K temperature of the grains. Recently, the radical–radical recombination (3) and (5) were suggested on grain surfaces[25] exploiting the gas grain warm-up chemical model.[35] However, the diffusion rates in the models have not been confirmed experimentally and were only guessed.

$$CH_3OCH_3 + CO \rightarrow CH_3COOCH_3 \quad (6)$$

As demonstrated above, the untangling of the formation routes to discrete isomers of $C_3H_6O_2$ has just scratched the surface, and none of the mechanisms proposed have been verified computationally or experimentally. On the other hand, bulk-ice chemistry has been demonstrated to form COMs carrying carbonyl (CO) functional groups *via* non-equilibrium chemistry.[2,16,20,36–39] In particular, Bennet *et al.* and Jones *et al.*[11,14,15,40–46] revealed that methanol (CH_3OH) is initially radiolyzed to methoxy radicals ($CH_3\dot{O}$) plus atomic hydrogen and hydroxymethyl radical ($\dot{C}H_2OH$) plus atomic hydrogen by proxies of galactic cosmic rays. Likewise, Kleimeier *et al.*[16,36,37,47] exposed that interstellar ices containing acetaldehyde (CH_3CHO) can store at least acetyl radicals ($CH_3\dot{C}O$). Consequently, hydroxyacetone (CH_3COCH_2OH, **1**) and methyl acetate (CH_3COOCH_3, **2**) are likely to be formed *via* radical–radical recombination reactions within interstellar ices (reactions (3) and (5)) (Fig. 2a). Note that methanol (CH_3OH) and acetaldehyde (CH_3CHO) have been detected on interstellar grains at fractions of up to 30% toward star-forming regions[48–51] and the low-mass protostar IRAS 16293-2422[52,53] and identified tentatively at levels of up to a few percent with respect to water,[54] respectively. Recently, acetaldehyde was reported as a key tracer of cosmic-ray-driven nonequilibrium chemistry leading to complex organics even deep within low-temperature interstellar ices.[20] Therefore, both methanol and acetaldehyde are viable precursors to hydroxyacetone (CH_3COCH_2OH, **1**) and methyl acetate (CH_3COOCH_3, **2**).

$$\dot{C}H_2OH + \dot{C}H_2CHO \rightarrow HCOCH_2CH_2OH \quad (7)$$

$$CH_3\dot{O} + \dot{C}H_2CHO \rightarrow HCOCH_2OCH_3 \quad (8)$$

In addition, keto–enol tautomerization of **1** and **2** can occur and their enols may also be formed. Here, isomer **1** can tautomerize to prop-1-ene-1,2-diol (**5**) and prop-2-ene-1,2-diol (**6**);[55] likewise, **2** can form 1-methoxyethen-1-ol (**7**) (Fig. 2a). Since the keto–enol tautomerism plays a fundamental role in the mechanism of biochemical processes such as the DNA mutagenesis,[56,57] those enols may contribute to the formation of molecular precursors linked to the origins of life, *e.g.*, isomer **6** can be formed *via* the dehydration involving the terminal OH group of glycerol.[58,59] Laboratory studies of interstellar analog ices have demonstrated the formation of enols – the thermodynamically less stable tautomers of aldehydes and ketones – in astrochemically relevant ice mixtures after the exposure of energetic electrons; these low temperature experiments detected vinyl alcohol (C_2H_3OH),[16,20] 1-propenol ($CH_3CHCH(OH)$),[20] 2-hydroxyacrylic acid ($CH_2(COH)$-COOH),[37] ethynol (HCCOH),[60] 1,2-ethenediol (HOCHCHOH)[45] and 1,1-ethenediol ($H_2CC(OH)_2$),[61] suggesting that enols should be ubiquitous in the interstellar medium.[16,45,61] However, only vinyl alcohol[62] and 1,2-ethenediol[63] have been detected in deep space so far. In organic synthesis, simple enols are usually regarded as short-lived species,[64] however, in enzymatic mechanisms, they are long-lived species playing key roles as intermediates.[65] Due to their reactivity with electrophiles, enols can play an important role in the formation of COMs linked to biomolecules, thus contributing to our understanding of the molecular complexity in the interstellar medium and in comets and meteorites.[45]

Here, we present laboratory experiments on the formation of hydroxyacetone (CH_3COCH_2OH, **1**), methyl acetate (CH_3COOCH_3, **2**) as well as their hitherto astronomically unobserved isomer 3-hydroxypropanal ($HCOCH_2CH_2OH$, **3**) in low-temperature interstellar model ices comprised of methanol (CH_3OH) and acetaldehyde (CH_3CHO) *via* reactions (3), (5) and (7), respectively (Fig. 2a), in simulation experiments replicating 'early' stages of molecular clouds of about 2×10^6 years; furthermore, their enol tautomers (**5–8**) were identified in the high dose experiments simulating 'aged' molecular cloud of typically 7×10^6 years.[66] The binary ice mixtures were irradiated at temperatures as low as 5 K with energetic electrons, which are utilized to simulate secondary electrons generated in the track of Galactic cosmic rays (GCRs) to initiate the non-equilibrium chemistry necessary to form COMs.[39] Our studies exploit the advantages of reflectron time-of-flight mass spectrometry coupled with fragment-free tunable photoionization (PI) as a sensitive, isomer-selective technique to unravel the complex chemistry taking place in the irradiated ices.[2,67,68] The subliming products can be probed *via isomer-specific* photoionization and detection as the irradiated ices are heated from 5 K to room temperature (temperature-programmed desorption, TPD). Combined with isotopic labeling of the parent molecules, detailed insights into the formation mechanism of distinct $C_3H_6O_2$ isomers are obtained. Our results contribute significantly to the understanding of formation pathways of multiple $C_3H_6O_2$ isomers detected in the ISM and to constraining fundamental astrochemical models and grain bulk ice chemistry on the formation of these species by implementing solid laboratory data, thus eventually expanding our knowledge on the evolution of organic matter and biorelevant molecules in space.

2. Experimental

2.1. Experimental strategy

Considering the molecular structure of isomers **1** and **2** along with their adiabatic ionization energies (IEs (Fig. 2a and Table S1, ESI†)), we pursue the following strategy to investigate their

formation in methanol–acetaldehyde ices. Upon interaction with energetic electrons, the methanol (CH_3OH) molecule can decompose *via* atomic hydrogen loss to the hydroxymethyl radical ($\dot{C}H_2OH$, **A**) and methoxy radical ($CH_3\dot{O}$, **B**);[40,43,44,46] likewise, the acetaldehyde (CH_3CHO) molecule can decompose *via* atomic hydrogen loss to the acetyl radical ($CH_3\dot{C}O$, **C**)[36] and – in principle – to the vinoxy radical ($\dot{C}H_2CHO$, **D**). Species **A–D** correspond to radicals containing distinct functional groups which are incorporated into products by recombination. Radical–radical recombination between the radical fragments of methanol (**A, B**) and of acetaldehyde (**C, D**) may yield hydroxyacetone (**1**; reaction (3)), methyl acetate (**2**; reaction (5)), 3-hydroxypropanal (**3**; reaction (7)), and/or 2-methoxy-acetaldehyde (**4**; reaction (8)), respectively (Fig. 2a). Based on the adiabatic ionization energies of **1–4**, three photon energies (10.49 eV, 9.70 eV, and 9.20 eV) were chosen in an attempt to distinguish and/or narrow down the isomers of $C_3H_6O_2$ (Fig. 3). At 10.49 eV, all isomers can be ionized; at 9.70 eV, only isomers **1a**, **2b**, and **4a–4c** can be ionized. At 9.20 eV, none of these isomers can be ionized. Due to the overlap of their ionization energies (Fig. 3), experiments with deuterated reactants are also required. Here, exploiting deuterated substitution experiments of CH_3OH–CD_3CHO and CD_3OH–CD_3CDO ices at these three photon energies critically assist in elucidating the dominant reaction mechanisms through the identification of $m/z = 77$ *versus* 76 and finding how their TPD profiles vary with the energy of the ionizing photons in the gas phase at 10.49 eV, 9.70 eV, and 9.20 eV (Fig. 2b, c and 4). Once the *primary products* are identified, experiments with increased irradiation dose are performed to study the formation of enols (**5–8**) at lower photon energies from 8.64 to 7.60 eV for the non-deuterated reactants; the exploitation of (partially) deuterated reactants in the identification of enols has to be avoided due to hydrogen *versus* deuterium scrambling at higher doses. Note that the computed IEs are also valid for (partially) deuterated products considering only slight changes in their ionization energies by less than 0.01 eV for the partially deuterated products.[36,69] The decrease of 0.03 eV for the IEs caused by the electric field of ion optics was considered during the IE error analysis (Table S1, ESI†).[70]

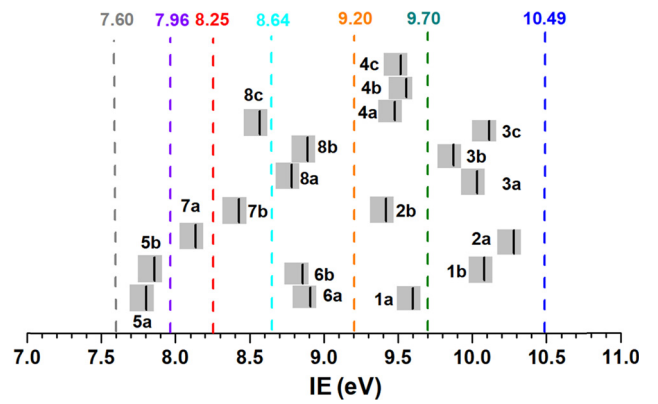

Fig. 3 The computed ionization energies of $C_3H_6O_2$ isomers (black solid line) and ranges (grey area) after error analysis (Table S1, ESI†). Seven VUV photon energies (dash lines) were used for the photoionization of sublimating molecules during the TPD process. Ionization energies for isomer 9 can be found in Table S1 (ESI†).

2.2. Experimental procedure

Experiments were conducted inside a stainless steel chamber under ultrahigh vacuum (UHV) conditions at pressures of a few 10^{-11} Torr at the W. M. Keck Research Laboratory in Astrochemistry.[71] A polished silver substrate was used for sample deposition and was interfaced to a two-stage closed-cycle helium refrigerator (Sumitomo Heavy Industries, RDK-415E) that can be freely rotated and translated vertically. The temperature of the silver substrate was monitored and regulated by a high-precision silicon diode and a programmable temperature controller to a precision of 0.1 K. The samples used in the experiment are isotopically labeled methanol (CD_3 CHO, Sigma Aldrich, ≥98 atom % D), unlabeled methanol (Sigma-Aldrich, HPLC grade), isotopically labeled acetaldehyde (CD_3CHO, CDN isotopes, ≥98 atom% D; CD_3CDO, Sigma Aldrich, ≥99 atom% D) and unlabeled acetaldehyde (Sigma Aldrich, anhydrous, ≥99.5% purity). Methanol and acetaldehyde samples were stored in separate glass vials interfaced to a high vacuum chamber and subjected to several freeze-thaw cycles using liquid nitrogen to remove residual atmospheric gases. After cooling the silver substrate to 5 K, methanol and acetaldehyde vapors were deposited exploiting separate glass capillary arrays. To achieve a ratio of methanol to acetaldehyde in the ice of 1 : 1, the partial pressures were chosen to be 2×10^{-8} Torr for both methanol and acetaldehyde during the deposition. The overall thickness of the ice was measured using a photodiode to record interference fringes between helium-neon laser (632.8 nm) reflections of the silver substrate and the ice surface.[72] A Fourier transform infrared (FTIR) spectrometer (Nicolet 6700) was utilized to probe the ices *in situ* in the range of 6000–500 cm^{-1} with 4 cm^{-1} spectral resolution before and after the deposition (Fig. 5 and 6). The concentration-weighted average between the refractive index of amorphous methanol ice ($n = 1.33 \pm 0.04$)[73] and that of acetaldehyde ($n = 1.303$)[74] of 1.32 ± 0.04 was used to derive the thickness of the ices from the interference fringes. The ice thicknesses of 740 ± 30 nm were determined by taking into account the density of methanol (0.779 g cm^{-3}) and acetaldehyde (0.787 g cm^{-3}).[75] Subsequently, the ice composition of methanol to acetaldehyde in the ice was determined to be $1.0 \pm 0.3 : 1$ by integrating the infrared features of acetaldehyde at 1128, 1350, and methanol at 2827, and 3270 cm^{-1} exploiting absorption coefficients of 6.6×10^{-19}, 1.1×10^{-18}, 5.3×10^{-18}, and 1.01×10^{-16} cm $molecule^{-1}$, respectively.[36,44,73,76] The results of this analysis are listed in Table 1 along with experimental parameters.

After the deposition, the mixed ice was then subjected to 5 keV electron irradiation over the entire sample for 15 minutes (low-dose) or 60 minutes (higher dose) at an irradiation current of 20 nA monitored by a Faraday cup before and after irradiation. These low-dose or higher dose irradiation conditions correspond to doses of 0.55 ± 0.09 or 2.2 ± 0.3 eV $molecule^{-1}$ for methanol and 0.81 ± 0.13 or 3.2 ± 0.6 eV $molecule^{-1}$ for acetaldehyde, respectively, according to Monte Carlo simulations carried out in the CASINO software suite.[77] The average

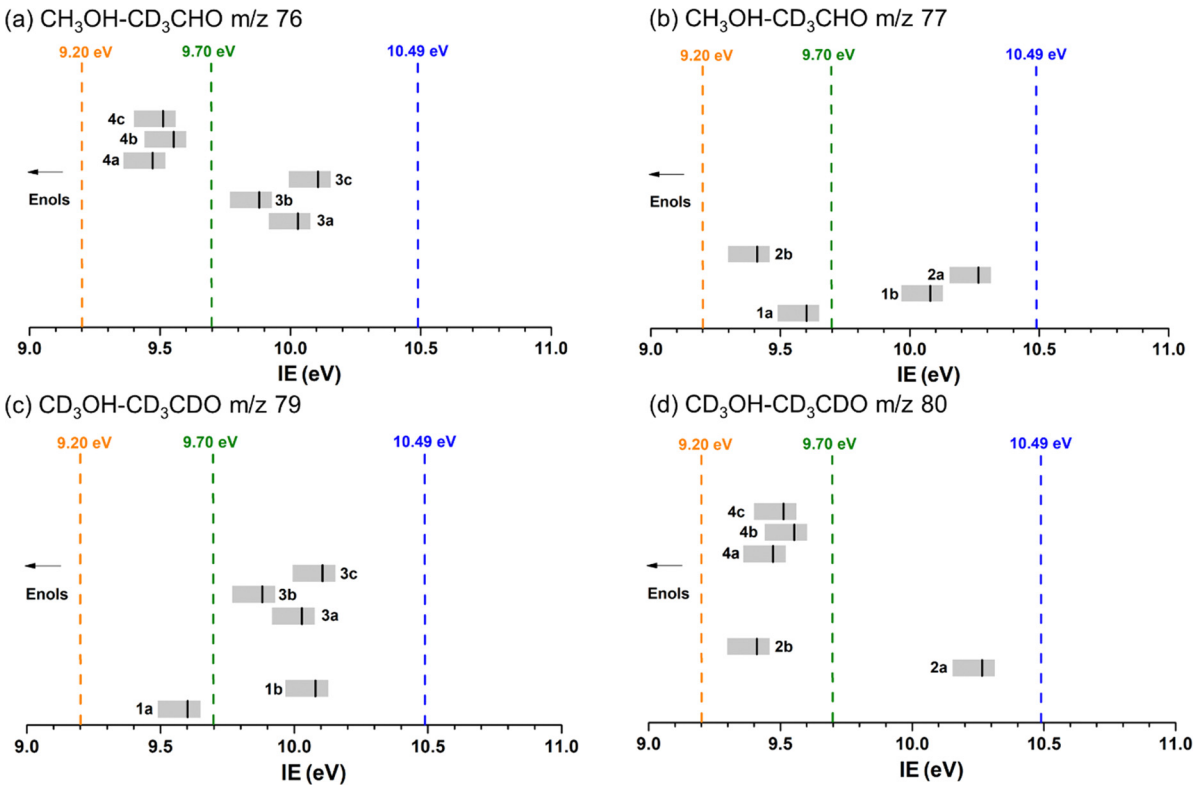

Fig. 4 Ionization energy ranges of isomers **1–4** in deuterated ice mixtures of $CH_3OH–CD_3CHO$ (a and b), and $CD_3OH–CD_3CDO$ (c and d). Three VUV photon energies (dash lines) were used for the photoionization of subliming molecules in these ices.

depths of 5 keV electrons of 330 ± 30 nm were calculated to be less than the thicknesses of the ices, which prevents electrons from reaching the silver substrate. Subsequent to the irradiation, temperature-programmed desorption (TPD) was conducted by heating the sample from 5 K to 320 K at a rate of 0.5 K minute^{-1}. The sublimed molecules from the sample were analyzed by vacuum ultraviolet (VUV) photoionization reflectron time-of-flight mass spectrometry (PI-ReToF-MS).

The tunable VUV photons (10.49 eV, 9.70 eV, 9.20 eV, 8.64 eV, 8.25 eV, 7.96 eV, and 7.60 eV) were generated by resonant or non-resonant four-wave mixing (FWM) of two synchronized pulsed laser beams from two dye lasers (Sirah, Cobra-Stretch) pumped by two Nd: YAG lasers (Spectra-Physics, Quanta Ray Pro 250-30 and 270-30) operating at a repetition rate of 30 Hz (Table 2). The 10.49 eV photons (118.222 nm) were generated by frequency tripling ($\omega_{vuv} = 3\omega_1$) of the third harmonic (355 nm) of the fundamental of an Nd: YAG laser in pulsed gas jets of Xe gas.[78] To produce 9.70 eV (127.819 nm) light, a second harmonic (532 nm) of an Nd:YAG laser was used to pump a Rhodamine 610/640 dye mixture to obtain 606.948 nm, which underwent third harmonic generation to produce ω_1 = 202.316 nm. A second Nd:YAG laser pumped a Coumarin 480 dye to obtain ω_2 = 484.982 nm, which then generated ω_{vuv} = 127.819 nm (9.70 eV) in a non-linear medium of Kr gas by combining with $2\omega_1$. The 9.20 eV (134.765 nm) and 8.64 eV (143.50 nm) light were produced by the difference FWM in pulsed gas jets of Xe gas with ω_1 = 222.566 nm and ω_2 = 638.667 nm (9.20 eV) or ω_2 = 495.679 nm (8.64 eV), respectively. The 222.566 nm was obtained *via* a double frequency of 445.132 nm from a dye laser pumped by an Nd: YAG laser (YAG B) (Table 2). The remaining three photon energies (8.25 eV, 7.96 eV and 7.60 eV) were generated by the difference FWM in pulsed gas jets of Xe gas with ω_1 = 249.628 nm and ω_2 = 736.448 nm (8.25 eV) or ω_2 = 628.232 nm (7.96 eV) or ω_2 = 532 nm (7.60 eV), respectively. The 249.628 nm was obtained *via* a double frequency of 499.256 nm from a dye laser pumped by an Nd: YAG laser (YAG B) (Table 2). The VUV light (ω_{vuv}) was spatially separated from the dye lasers (ω_1 and ω_2) using a biconvex lithium fluoride (LiF) lens (ISP Optics) in an off-axis geometry and then focused at 2 mm above the silver substrate to ionize subliming molecules. The resulting ions were then analyzed by a ReToF-MS (Jordan TOF Products, Inc.) according to their arrival times in bins 3.2 ns wide. The signal was amplified with a fast preamplifier (Ortec 9305) and recorded with a dedicated multi-channel scaler (FAST ComTec, MCS6A) with accumulation times of 2 minutes (3600 sweeps) for each recorded mass spectra in 0.5 K min^{-1} during the temperature-programmed desorption (TPD) phase.

2.3. Computational details

Geometries of various $C_3H_6O_2$ isomers, which can potentially form in the acetaldehyde/methanol mixed ices, including methyl acetate, hydroxypropanones, hydroxypropanals, propenediols, methoxyacetaldehydes, and methoxyethenols, as well as their cations, were optimized using the long-range corrected hybrid ωB97XD density functional[79] with Dunning's correlation-consistent triple-ζ cc-pVTZ basis set.[80] The same ωB97XD/cc-pVTZ theoretical approach was

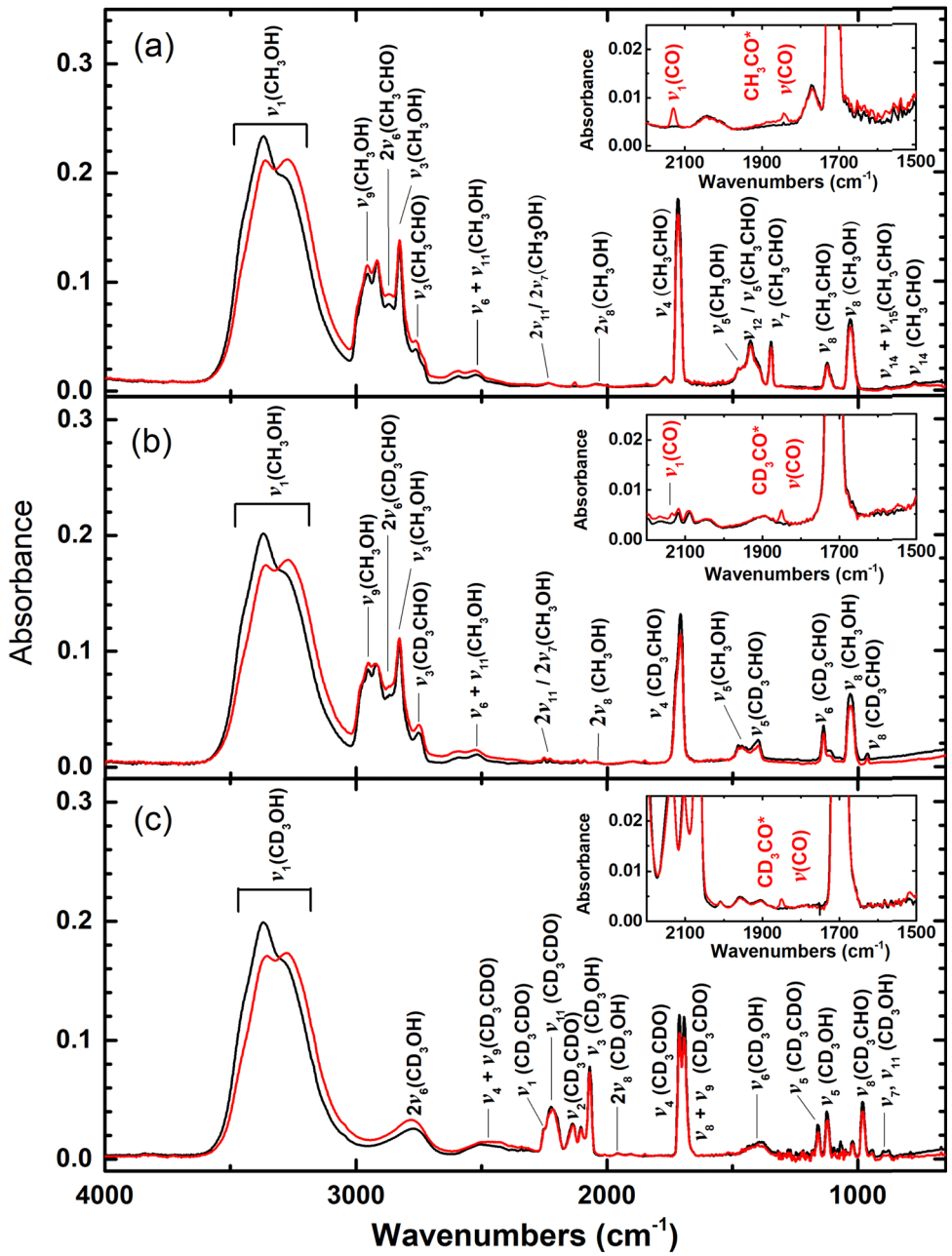

Fig. 5 FTIR spectra of methanol (CH_3OH) and acetaldehyde (CH_3CHO) ices at 5 K before (black line) and after (red line) irradiation for 15 minutes: (a) CH_3OH–CH_3CHO, (b) CH_3OH–CD_3CHO, and (c) CD_3OH–CD_3CDO. For clarity, only significant peaks are labelled; detailed assignments are compiled in Tables 3–5. Inset: Zoom in between 2200 and 1500 cm^{-1} showing new peaks after irradiation corresponding to carbon monoxide and the acetyl radical.

also applied for calculating their vibrational frequencies and zero-point vibrational energy corrections (ZPE). Single-point energies of the optimized neutral $C_3H_6O_2$ molecules and corresponding cations were subsequently refined employing explicitly correlated coupled cluster theory at the RCCSD(T)-F12b level[81,82] which includes single and double excitations with perturbative treatment of triple excitations, with Dunning's triple-ζ cc-pVTZ-F12 basis set. The RCCSD(T)-F12b/cc-pVTZ-F12 single-point energies with ωB97XD/cc-pVTZ ZPE corrections were used to evaluate relative energies and adiabatic ionization energies (AIE) of the neutral $C_3H_6O_2$ species. The expected accuracy of the RCCSD(T)-F12b/cc-pVTZ-F12//ωB97XD/cc-pVTZ+ZPE(ωB97XD/cc-pVTZ) computational scheme is within 0.01–0.02 Å for bond lengths, 1°–2° for bond angles, about 0.05 eV for AIE.[83] This value is close to the combined error limit (0.08 eV) after taking into account the measured experimental ionization energies (Table S1, ESI†). The Gaussian 16[84] and MOLPRO 2021[85] quantum chemistry software packages were utilized for the ωB97XD and RCCSD(T)-F12b electronic structure calculations, respectively. The computed Cartesian coordinates and vibration frequencies are listed in Table S2 (ESI†).

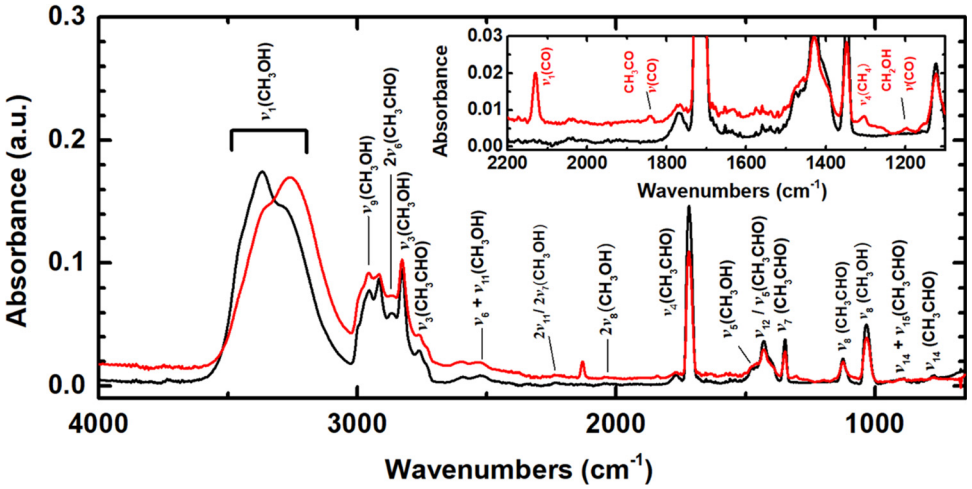

Fig. 6 FTIR spectra of CH_3OH–CH_3CHO ices at 5 K before (black line) and after (red line) irradiation for 60 minutes. Inset: Zoom in between 2200 and 1100 cm^{-1} showing new peaks after irradiation.

Table 1 Conditions of ices studied in the experiment including the composition, ice thickness, irradiation parameters, and VUV photon energy

Ice	Composition of methanol: acetaldehyde	Thickness (nm)	Current (nA)	Irradiation time (s)	Dose (eV/CH_3OH)	Dose (eV/CH_3CHO)	Photon energy (eV)
CH_3OH–CH_3CHO	0.9 ± 0.3 : 1	770 ± 30	—	—	—	—	10.49
CH_3OH–CH_3CHO	0.9 ± 0.3 : 1	740 ± 30	20 ± 2	900 ± 10	0.55 ± 0.09	0.81 ± 0.13	10.49
CD_3OH–CD_3CDO	1.1 ± 0.2 : 1	770 ± 30	—	—	—	—	10.49
CD_3OH–CD_3CDO	1.3 ± 0.2 : 1	720 ± 30	20 ± 2	900 ± 10	0.57 ± 0.09	078 ± 0.13	10.49
CH_3OH–CD_3CHO	1.0 ± 0.3 : 1	720 ± 30	—	—	—	—	10.49
CH_3OH–CD_3CHO	1.3 ± 0.3 : 1	790 ± 30	19 ± 3	900 ± 10	0.52 ± 0.11	0.73 ± 0.15	10.49
CH_3OH–CH_3CHO	1.0 ± 0.3 : 1	740 ± 30	20 ± 2	900 ± 10	0.55 ± 0.09	0.81 ± 0.13	9.70
CD_3OH–CD_3CDO	1.3 ± 0.2 : 1	720 ± 30	21 ± 1	900 ± 10	0.60 ± 0.08	0.82 ± 0.11	9.70
CH_3OH–CD_3CHO	1.0 ± 0.1 : 1	720 ± 30	21 ± 3	900 ± 10	0.58 ± 0.11	0.80 ± 0.15	9.70
CH_3OH–CH_3CHO	1.1 ± 0.3 : 1	740 ± 30	21 ± 3	900 ± 10	0.58 ± 0.11	0.85 ± 0.16	9.20
CD_3OH–CD_3CDO	0.8 ± 0.1 : 1	770 ± 30	19 ± 3	900 ± 10	0.54 ± 0.11	0.74 ± 0.15	9.20
CH_3OH–CD_3CHO	1.4 ± 0.2 : 1	790 ± 30	18 ± 4	900 ± 10	0.49 ± 0.13	0.69 ± 0.17	9.20
CH_3OH–CH_3CHO	0.9 ± 0.3 : 1	720 ± 30	20 ± 1	3600 ± 10	2.2 ± 0.3	3.2 ± 0.4	9.20
CH_3OH–CH_3CHO	1.3 ± 0.2 : 1	720 ± 30	20 ± 3	3600 ± 10	2.2 ± 0.3	3.2 ± 0.6	8.64
CH_3OH–CH_3CHO	0.9 ± 0.3 : 1	720 ± 30	20 ± 3	3600 ± 10	2.2 ± 0.3	3.2 ± 0.6	8.25
CH_3OH–CH_3CHO	0.9 ± 0.4 : 1	720 ± 30	20 ± 3	3600 ± 10	2.2 ± 0.3	3.2 ± 0.6	7.96
CH_3OH–CH_3CHO	1.1 ± 0.3 : 1	740 ± 30	20 ± 4	3600 ± 10	2.2 ± 0.5	3.2 ± 0.8	7.60

3. Results & discussion

3.1 FTIR

Fourier transform infrared (FTIR) spectroscopy was utilized to monitor the chemical evolution of the CH_3OH–CH_3CHO ice as well as its isotopically labeled systems (CH_3OH–CD_3CHO, CD_3OH–CD_3CDO) before (black line) and after (red line) the exposure to the energetic electrons (Fig. 5 and 6). Detailed assignments of the FTIR spectra are summarized in Tables 3–6. Prior to the electron irradiation, the absorptions in the infrared spectra can be attributed to the fundamentals of the methanol and acetaldehyde as indicated through the black labels in Fig. 5 and 6. The spectra of the unprocessed ices revealed prominent absorptions (Fig. 5a and Table 3) of methanol such as the broad O–H stretching mode (3020–3600 cm^{-1}; ν_1), C–H stretching fundamental (2993 cm^{-1}; ν_2), the symmetric stretching modes of the methyl group (2956 cm^{-1}, ν_9; 2828 cm^{-1}, ν_3), the C–H bending mode (1455 cm^{-1}; ν_5), and the C–O stretching mode (1030 cm^{-1}; ν_8);[42,45,46] intense absorptions of acetaldehyde such as the overtone mode (2865 cm^{-1}; $2\nu_6$), stretching mode of the carbonyl moiety (1718 cm^{-1}; ν_4), and $\gamma_r(CH_3)$ (1123 cm^{-1}; $2\nu_8$)[16,47] are also prominent.

After the irradiation (red lines; Fig. 5), the absorbance features of methanol (ν_1, ν_3, ν_4, and ν_8) and acetaldehyde (ν_3, ν_4, ν_7, and ν_8) decreased by (7 ± 6) % and (7 ± 5) %, respectively. In addition, new absorption features arose at 2130 cm^{-1} and 1840 cm^{-1} indicating the CO stretch (2129 cm^{-1}; ν_1) of carbon monoxide (CO) and the acetyl radical ($CH_3\dot{C}O$, ν(C═O)),[16,36,86] respectively (insets of Fig. 5 and 6). Furthermore, the acetyl-d_3 radical ($CD_3\dot{C}O$) is observed at 1850 cm^{-1} in both deuterated ice mixtures (Fig. 5 and Tables 4, 5) thus confirming the assignment of the acetyl radical ($CH_3\dot{C}O$) in the CH_3OH–CH_3CHO ice.[16,47] We noticed that the absorptions of vinoxy radical ($\dot{C}H_2CHO$) were reported to be at 1525 cm^{-1} and 1541 cm^{-1} and those of

Table 2 Parameters for the generation of vacuum ultraviolet (VUV) light[a]

VUV	Photoionization energy (eV)	10.49 ($3\omega_1$)	9.70 ($2\omega_1$–ω_2)	9.20 ($2\omega_1$–ω_2)	8.64 ($2\omega_1$–ω_2)	8.25 ($2\omega_1$–ω_2)	7.96 ($2\omega_1$–ω_2)	7.60 ($2\omega_1$–ω_2)
	Wavelength (nm)	118.222	127.819	134. 765	143.50	150.284	155.759	163.073
ω_1	Wavelength (nm)	355	202.316	222.566	222.566	249.628	249.628	249.628
Nd:YAG	Wavelength (nm)	355	532	355	355	355	355	355
Dye laser	Wavelength (nm)	—	606.948	445.132	445.132	499.256	499.256	499.256
Dye		—	Rhodamine 610 and 640	Coumarin 450	Coumarin 450	Coumarin 503	Coumarin 503	Coumarin 503
ω_2	Wavelength (nm)	—	484.982	638.667	495.679	736.448	628.232	—
Nd:YAG	Wavelength (nm)	—	355	532	355	532	532	532
Dye laser	Wavelength (nm)	—	484.982	638.667	495.679	736.448	628.232	—
Dye		—	Coumarin 480	DCM and DMSO	Coumarin 480	LDS 722	Rhodamine 640	—
	Nonlinear medium	Xenon	Krypton	Xenon	Xenon	Xenon	Xenon	Xenon

[a] The uncertainty for VUV photon energies is less than 0.005 eV.

vinoxy-d_2 ($\dot{C}D_2CHO$) at 1534 cm^{-1} and 1537 cm^{-1},[86] however, there is no obvious peak observed in the infrared spectra (Fig. 5). Isotopic experiments with deuterium-(D-) precursors in the ices revealed red shifts of hydrogen-bearing functional groups (Fig. 5b, c and Tables 4, 5). Furthermore, after the irradiation for 60 minutes in the CH_3OH–CH_3CHO ice, two new absorption features arose at 1304 cm^{-1} and 1197 cm^{-1} indicating the deformation mode of methane (CH_4; ν_4) and the hydroxymethyl radical ($\dot{C}H_2OH$; ν_6).[45] Due to the overlapping IR features, no conclusive fundamentals of prospective reaction products **(1–8)** could be identified uniquely from FTIR spectra highlighting that an additional experimental technique is needed to detect the individual reaction products.[2]

3.2 PI-ReTOF-MS

The PI-ReTOF-MS technique allows for the isomer-specific identification of reaction products based on their desorption temperatures and ionization energies.[2,87,88] This is exploited here to identify individual $C_3H_6O_2$ isomers formed after electron irradiation in CH_3OH–CH_3CHO as well as its deuterated ices (CH_3OH–CD_3CHO; CD_3OH–CD_3CDO) based on their ionization energies and mass-to-charge ratios (m/z) (Fig. 2a–c, 3 and 4). The PI-ReTOF mass spectra of the photoionized desorbed molecules from the irradiated ice mixtures are compiled in Fig. 7–11. Initially, three photon energies (10.49 eV, 9.70 eV, and 9.20 eV) were selected to distinguish isomers **1–4** formed *via* radical–radical recombination after *low-dose* irradiation (Fig. 3 and 4). Focusing on the $C_3H_6O_2$ isomers, the TPD profile of ions at m/z = 74 for CH_3OH–CH_3CHO ice at 10.49 eV (Fig. 9a) shows two prominent sublimation events: a low-intensity peak at 130 K (Peak 1) and a higher intensity event at 179 K (Peak 2). Peak 2 transitions to a broad, poorly defined low-intensity shoulder region that continues to 250 K; this shoulder region is hereafter

Table 3 Absorption peaks observed in CH_3OH–CH_3CHO ices before and after electron irradiation for 15 minutes at 5 K[a]

Before irradiation (cm^{-1})		New absorption after irradiation (cm^{-1})	Assignment
CH_3OH	CH_3CHO		
3402, 3261, 3048			ν_1
2993			ν_2
2956			ν_9
2920			$2\nu_4/2\nu_5/2\nu_{10}$
	2865		$2\nu_6$
2828			ν_3
	2759		ν_3
2600			$\nu_4 + \nu_{11}/\nu_7 + \nu_4/\nu_6/\nu_{10}$
2525			$\nu_6 + \nu_{11}$
2237			$2\nu_{11}/2\nu_7$
		2130	ν_1 (CO)
2042			$2\nu_8$
		1840	$CH_3C\dot{O}$ ν(CO)
	1769		$2\nu_9$
	1718		ν_4
1478			ν_4
1455			ν_5
	1430		ν_{12}/ν_5
	1392		ν_6
	1347		ν_7
	1123		ν_8
1030			ν_8
	886		$\nu_{14} + \nu_{15}$
	772		ν_{14}

[a] Assignments based on ref. 42, 45, 47 and 102.

Table 4 Absorption peaks observed in CH_3OH–CD_3CHO ices before and after electron irradiation for 15 minutes at 5 K[a]

Before irradiation (cm^{-1})		New absorption after irradiation (cm^{-1})	Assignment
CH_3OH	CD_3CHO		
3402, 3261, 3048			ν_1
2993			ν_2
2956			ν_9
2920			$2\nu_4/2\nu_5/2\nu_{10}$
	2864		$2\nu_6$
2828			ν_3
	2754		ν_3
2600			$\nu_4 + \nu_{11}/\nu_7 + \nu_4/\nu_6/\nu_{10}$
2525			$\nu_6 + \nu_{11}$
2237			$2\nu_{11}/2\nu_7$
	2225		ν_2
		2130	ν_1 (CO)
	2118		ν_3
	2085		$\nu_6 + \nu_8$
2042			$2\nu_8$
	1890		$\nu_6 + \nu_9$
		1850	$CD_3C\dot{O}$ ν(CO)
	1711		ν_4
1478			ν_4
1455			ν_5
	1397		ν_5
	1138		ν_6
1030			ν_8
	963		ν_8

[a] Assignments based on ref. 42, 45, 47, 102.

Table 5 Absorption peaks observed in CD_3OH–CD_3CDO ices before and after electron irradiation for 15 minutes at 5 K[a]

Before irradiation (cm^{-1})		New absorption after irradiation (cm^{-1})	Assignment
CD_3OH	CD_3CDO		
3364, 3267			ν_1
2779			$2\nu_6$
	2472		$\nu_4 + \nu_9$
	2312		$2\nu_5$
	2254		ν_1
	2219		ν_{11}
	2134		ν_2
	2104		ν_2
2070			ν_3
1958			$2\nu_8$
	1908		$\nu_5 + \nu_9$
		1850	$CD_3C\dot{O}$ ν(CO)
	1711		ν_4
	1693		$\nu_8 + \nu_9$
1414			ν_6
	1157		ν_5
1121			ν_5
	1021		ν_6
987			ν_8
	941		ν_8
898			ν_7, ν_{11}

[a] Assignments based on ref. 16, 43, 103.

Table 6 Absorption peaks observed in CH_3OH–CH_3CHO ices before and after electron irradiation for 60 minutes at 5 K[a]

Before irradiation (cm^{-1})		New absorption after irradiation (cm^{-1})	Assignment
CH_3OH	CH_3CHO		
3402, 3261, 3048			ν_1
2993			ν_2
2956			ν_9
2920			$2\nu_4/2\nu_5/2\nu_{10}$
	2865		$2\nu_6$
2828			ν_3
	2759		ν_3
2600			$\nu_4 + \nu_{11}/\nu_7 + \nu_4/\nu_6/\nu_{10}$
2525			$\nu_6 + \nu_{11}$
2237			$2\nu_{11}/2\nu_7$
		2130	ν_1 (CO)
2042			$2\nu_8$
		1840	$CH_3C\dot{O}$ ν(CO)
	1769		$2\nu_9$
	1718		ν_4
1478			ν_4
1455			ν_5
	1430		ν_{12}/ν_5
	1392		ν_6
	1347		ν_7
		1304	ν_4 (CH_4)
		1197	ν_6 ($\dot{C}H_2OH$)
	1123		ν_8
1030			ν_8
	886		$\nu_{14} + \nu_{15}$
	772		ν_{14}

[a] Assignments based on ref. 42, 45, 47, 102.

designated as Peak 3. The signal belonging to m/z = 74 can be associated with $C_2H_2O_3$, $C_3H_6O_2$, $C_4H_{10}O$, and C_6H_2, it is imperative to confirm the molecular formula using isotopically-labeled precursors. The substitution of CH_3CHO (Fig. 2a) by CD_3CHO (Fig. 2b) results in products with two or three deuterium atoms ($C_3H_4D_2O_2$ and $C_3H_3D_3O_2$) that can be observed at m/z = 76 and at m/z = 77, respectively, in the CH_3OH–CD_3CHO ice (Fig. 9b and c). Similarly, an additional deuterated ice CD_3OH–CD_3CDO (Fig. 2c) results in products with five and six deuterium atoms ($C_3HD_5O_2$ and $C_3D_6O_2$); the observed signals shift to m/z = 79 and m/z = 80, respectively (Fig. 9d and e). In each case, the TPD profiles are observed at corresponding temperatures and overlap validating the assignment of products of the molecular formula $C_3H_6O_2$ for each profile.

3.2.1 Low-dose experiments

3.2.1.1 CH_3OH–CH_3CHO Ice. As previously mentioned, the TPD profile of m/z = 74 ($C_3H_6O_2$) at 10.49 eV in the CH_3OH–CH_3CHO ice (Fig. 9a) reveals peaks at 130 K (Peak 1) and 179 K (Peak 2), as well as a broad shoulder extending to a maximum of 250 K (Peak 3). A blank experiment (gray line) was conducted under identical conditions, but without electron irradiation of the ices to verify that the peaks result from irradiation; no signal was observed in this blank experiment confirming that peaks 1 to 3 are the result of the irradiation exposure of the ices. At 10.49 eV (blue line), all $C_3H_6O_2$ isomers can be ionized according to the computed and experimental ionization energies (Table S1 and Fig. 3, 4, ESI†). Therefore, these two peaks can be associated with any isomers **1–4** (Fig. 3). In addition, keto-enol tautomerization reaction can occur in the irradiated ices as shown previously by Kleimeier *et al.*[16,61] and thus their enol products may also be detected at 10.49 eV. Thereafter, the photon energy was reduced to 9.70 eV; at this energy, isomers/conformers **1b, 2a,** and **3a–3c** cannot be ionized (Fig. 3). Upon reducing the photon energy to 9.70 eV (green line), Peak 1 is absent and Peak 2 is significantly lowered in intensity; still, ion signal at m/z = 74 reveals Peak 3 as a broad sublimation event from 160 to 250 K. Therefore, Peak 1 can be linked to **1b, 2a,** and/or **3a–3c**, whereas Peaks 2 and 3 might be connected to **1a**, **2b**, **4**, and/or enols (Fig. 3). The difference between in ion counts of 10.49 eV minus 9.70 eV is shown as an insert in Fig. 9a. Recall that since 9.70 eV photons cannot ionize **1b**, **2a**, and **3a–c** (IE = 9.77–10.32 eV), ion signal of Peak 1 and Peak 2 can be associated with these isomers. Essentially, peak 3 remains after tuning the photon energy to 9.20 eV (yellow line), but isomers **1–4** cannot be ionized at this photon energy (Fig. 3). Therefore, the broad Peak 3 can only result from enols **5–8** (IE = 7.70–8.98 eV), for which adiabatic ionization energies are lower than 9.20 eV (Table S1, ESI†). Since the TPD profiles overlap satisfactorily at 9.70 and 9.20 eV, this suggests that **1a**, **2b**, and **4** (IE = 9.30–9.65 eV) were likely not formed.

3.2.1.2 CH_3OH–CD_3CHO Ice. The deuterated CH_3OH–CD_3CHO ice experiment (Fig. 2b) generates TPD profiles at m/z = 76 ($C_3H_4D_2O_2$, Fig. 9b) and m/z = 77 ($C_3H_3D_3O_2$, Fig. 9c). For m/z = 76 at 10.49 eV (Fig. 9b), the TPD profile shows peaks at 131 K (Peak 1), and more intense peak at 180 K (Peak 2) with signal extending to 250 K (Peak 3). Given the possible reactions leading to m/z = 76 in Fig. 2b, the candidates for these peaks are **3**, **4**, and enols (Fig. 4a). Utilizing a photon energy of 9.70 eV, so that isomer **3** cannot be ionized, Peak 1 and the shoulder at

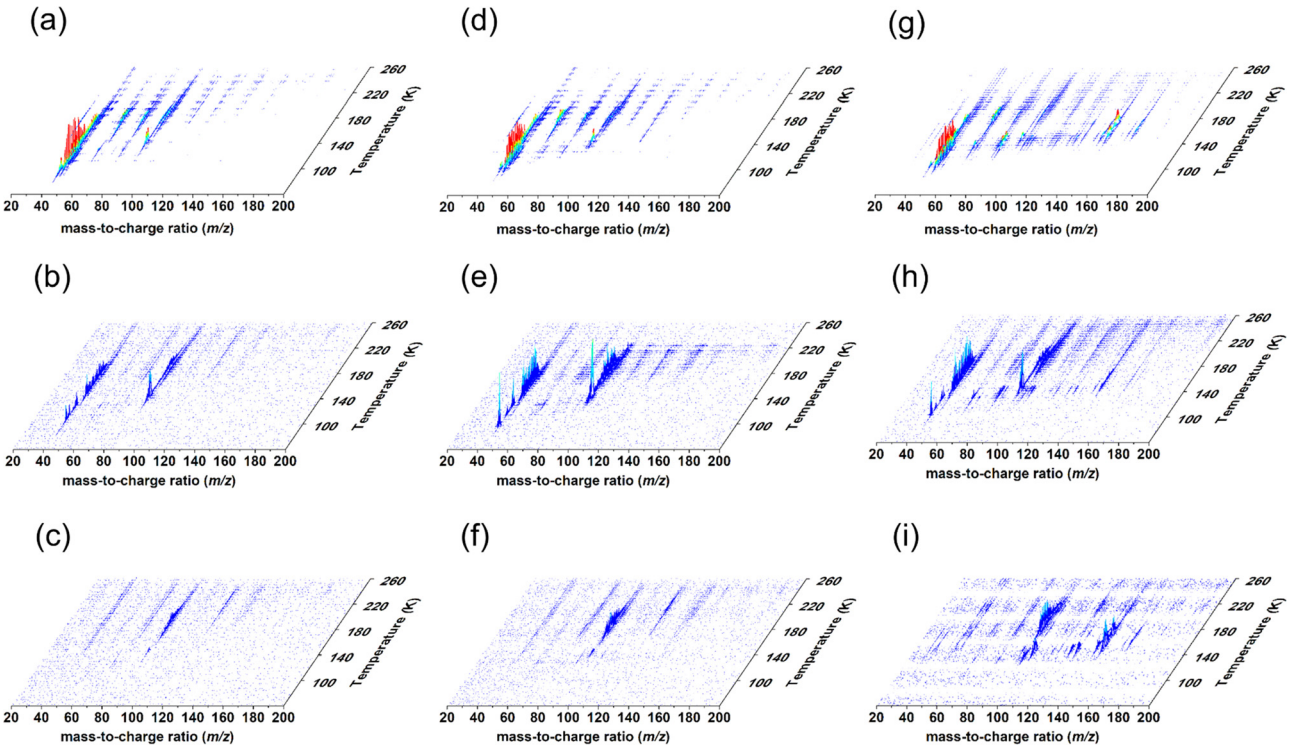

Fig. 7 PI-ReTOF-MS mass spectra measured during the temperature programmed desorption (TPD) phase of the irradiated methanol–acetaldehyde ice mixtures for 15 minutes: CH_3OH–CH_3CHO ice photoionized at 10.49 eV (a), 9.70 eV (b) and 9.20 eV (c); CH_3OH–CD_3CHO ice photoionized at 10.49 eV (d), 9.70 eV (e) and 9.20 eV (f); CD_3OH–CD_3CDO ice photoionized at 10.49 eV (g), 9.70 eV (h) and 9.20 eV (i).

194 K vanish leaving only a peak at 180 K with low intensity extending to 225 K. Consequently, the difference of ion signal between 10.49 eV and 9.70 eV (Fig. 9b, inset) must be linked to **3** (IE = 9.77–10.16 eV). Due to the overlap of the ionization energies of **3a–3c** (Fig. 3), no attempt was made to discriminate between the **3a**, **3b**, or **3c** conformers. Upon lowering the photon energy to 9.20 eV the TPD profile matches well with that for 9.70 eV, suggesting once again that isomer **4** (IE = 9.36–9.60 eV) was not formed; hence the remaining signal from 160 to 250 K is linked to Peak 3 and the formation of enols.

For m/z = 77 (Fig. 9c), the TPD profile collected at a photon energy of 10.49 eV reveals two peaks at 131 K (Peak 1) and 179 K (Peak 2) with lower intensity signal continuing to 250 K (Peak 3), suggesting the formation of **1**, **2**, and/or enols (Fig. 2b and 4b).

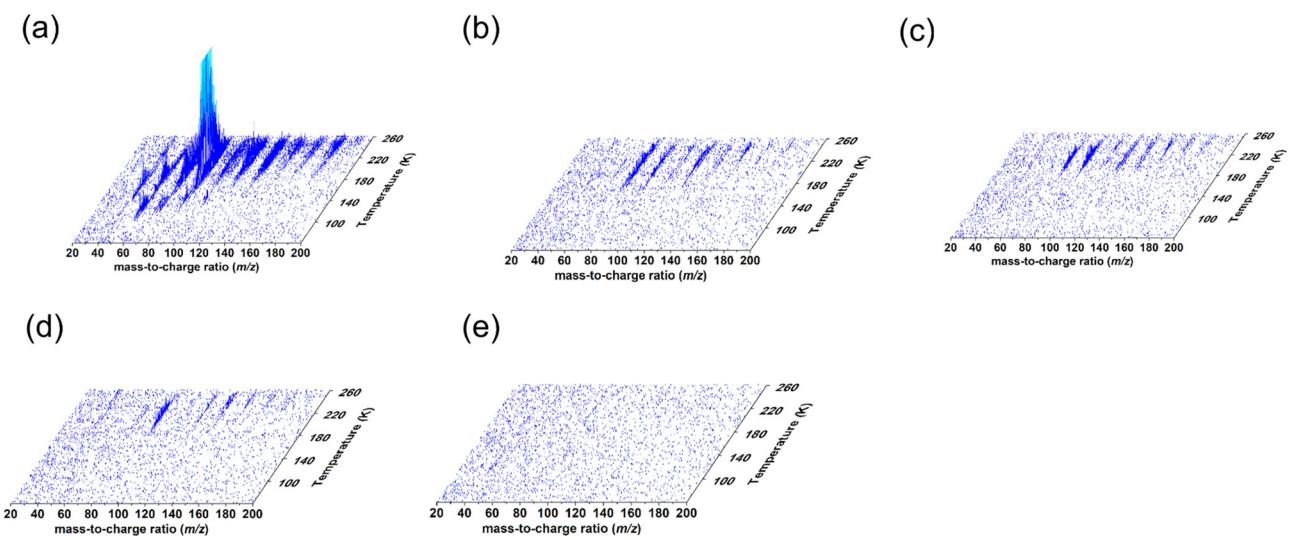

Fig. 8 PI-ReTOF-MS mass spectra measured during the TPD phase of the CH_3OH–CH_3CHO ice after higher dose irradiation photoionized at 9.20 eV (a), 8.64 eV (b), 8.25 eV (c), 7.96 eV (d) and 7.60 eV (e).

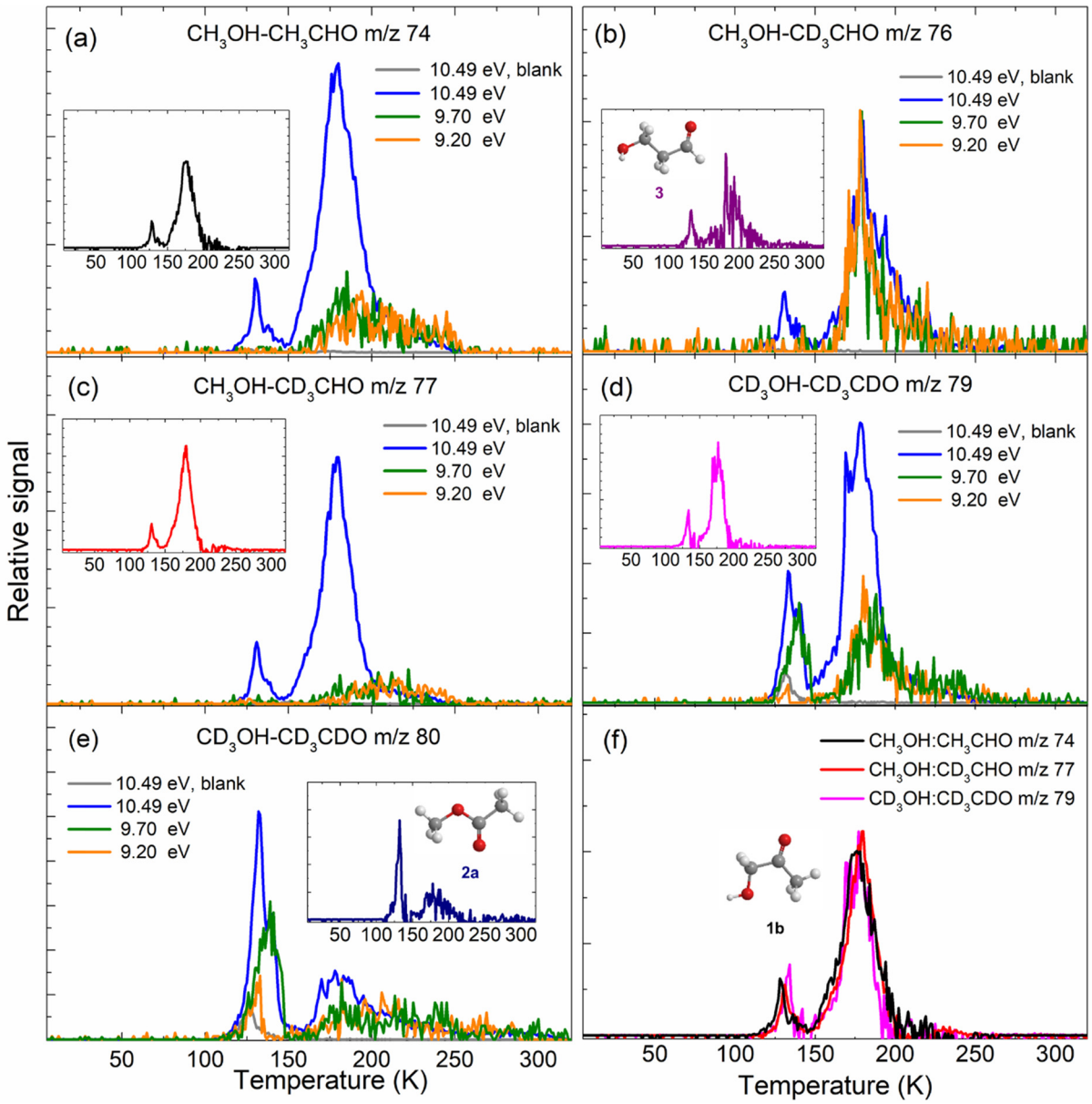

Fig. 9 PI-ReTOF-MS data during the TPD phase of CH_3OH–CH_3CHO ice at m/z = 74 (a), CH_3OH–CD_3CHO ice at m/z = 76 and 77 (b and c), and CD_3OH–CD_3CDO ice at m/z = 79 and 80 (d and e) photo-ionized with photon energies of 10.49 eV (grey and blue), 9.7 eV (green), and 9.2 eV (yellow), respectively. The inset figures show the difference in TPD profiles of 10.49 eV (blue) and 9.7 eV (green).

In the TPD profiles at both 9.70 and 9.20 eV, Peak 1 and Peak 2 are not present, but Peak 3 remains. By comparing the TPD profiles with photon energy at 10.49 eV and 9.70 eV, the difference in TPD profiles shows Peak 1 and Peak 2 (Fig. 9b, inset), which are linked to **1b** and/or **2a** (IE = 9.97–10.32 eV, Fig. 4b). Because the TPD profiles for 9.70 and 9.20 eV match well, the signal is assigned to one or more of the enols while isomers **1a** and **2b** (IE = 9.30–9.65 eV) did not form (Fig. 4b).

3.2.1.3 CD_3OH–CD_3CDO Ice. The deuterated CD_3OH–CD_3CDO ice experiment generates TPD profiles at m/z = 79 ($C_3HD_5O_2$, Fig. 9d) and m/z = 80 ($C_3D_6O_2$, Fig. 9e). For m/z = 79 (Fig. 9d) at 10.49 eV photoionization, the TPD profile shows peaks at 133 K (Peak 1), a more intense peak at 178 K extending to 250 K. Given the possible reactions leading to m/z = 79 in Fig. 2c, the candidates for these peaks are **1**, **3**, and enols (Fig. 4c). We then reduced the photon energy to 9.70 eV at which **1b** and **3** (IE = 9.77–10.16 eV) cannot be ionized. Therefore, the two sublimation events at 9.70 eV peaking at 139 K and 187 K must link to **1a** and/or enols. However, the aforementioned experiments discounted **1a**; hence this signal is most likely linked to enols. The difference in TPD profiles between 10.49 eV and 9.70 eV trace Peak 1 and Peak 2 (Fig. 9d, inset), which are connected to **1b** and/or **3** (Fig. 4c). Further reducing the photon energy to 9.20 eV results in a sublimation event of 155–250 K which matches well with the results at 9.70 eV, once again suggesting **1a** was not formed (Fig. 4c).

For ion signals of m/z = 80 (Fig. 9e), the TPD profile at 10.49 eV shows an intense peak at 132 K (Peak 1) and a broad

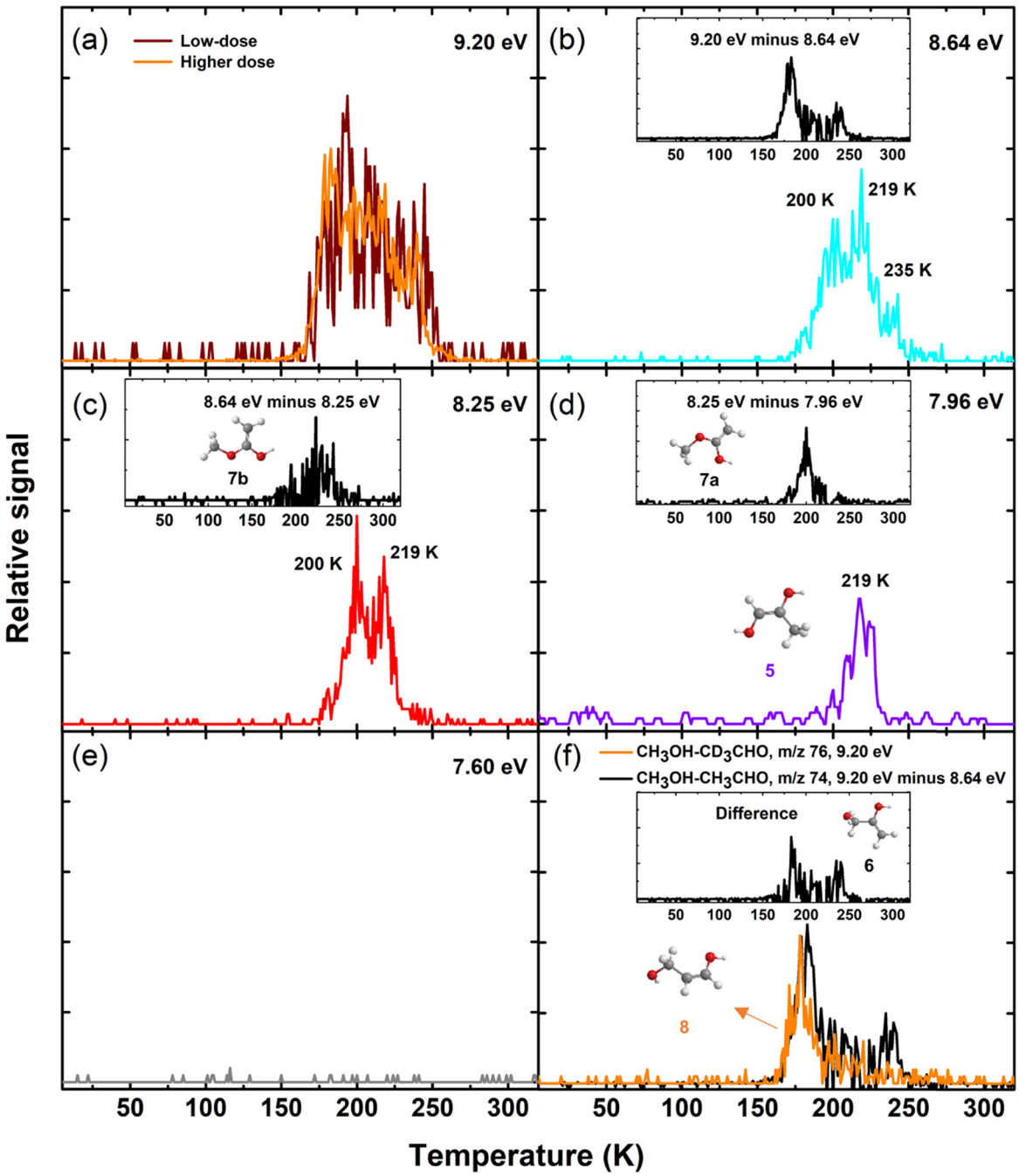

Fig. 10 PI-ReTOF-MS data during the TPD phase of CH_3OH–CH_3CHO ice at m/z = 74 photo-ionized at photon energies of 9.20 eV (a), 8.64 eV (b), 8.25 eV (c), 7.96 eV (d) and 7.60 eV (e), as well as the overlay of TPD profiles for m/z = 76 in CH_3OH–CD_3CHO ice at 9.20 eV and the subtraction of TPD profiles between 9.20 eV and 8.64 eV at m/z = 74 in CH_3OH–CH_3CHO ice (f). The inset figures show the difference in TPD profiles.

peak at 178 K with a signal extending to 250 K. These data suggest the formation of **2**, **4**, and/or enols (Fig. 2c and 4d). We then lowered the photon energy to 9.70 eV, at which **2a** (IE = 10.25 ± 0.05 eV) cannot be ionized. The difference in TPD profiles between 10.49 eV and 9.70 eV exhibits sublimation events from 110 to 150 K and 160 to 220 K (Fig. 9e, inset) thus confirming the formation of **2a**. By further reducing the photon energy to 9.20 eV, the broad sublimation event from 160 K to 250 K remains; hence, it can only be linked to enols. The TPD profiles for 9.70 and 9.20 eV match well for the sublimation events after 160 K; this indicates that **2b** and **4** were not found, which agrees with the results discussed above.

Fig. 9f shows the differences in TPD profiles between 10.49 eV and 9.70 eV in CH_3OH–CH_3CHO (m/z = 74), CH_3OH–CD_3CHO (m/z = 77), and CD_3OH–CD_3CDO (m/z = 79) ices. The overlay of three TPD profiles matches quite well for Peak 1 and Peak 2, suggesting both peaks are linked to the same isomer. As discussed above, the ion signal at m/z = 74 is linked to **1b**, **2a**,

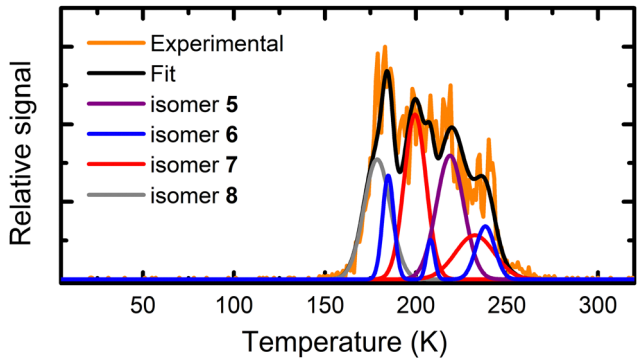

Fig. 11 PI-ReTOF-MS data at m/z = 74 during the TPD phase TPD profile of CH_3OH–CD_3CHO ice after higher dose irradiation of ices with photon energies of 9.20 eV, and the deconvolution of distinct isomers. The fitting curves (red) peaking at 200 K and 235 K correspond to **7a** and **7b**, respectively.

and/or **3** (IE = 9.77–10.32 eV, Fig. 3). Isomers **1b** and/or **2a** (IE = 9.97–10.32 eV) can contribute to the ion signal at m/z = 77 (Fig. 4b), and **1b** and/or **3** (IE = 9.77–10.16 eV) for the ion signal at m/z = 79 (Fig. 4c). Since only **1b** is present in all three schemes, these two sublimation events suggest the formation of isomer **1b**.

3.2.1.4 Conclusion: low dose experiments. Overall, the aforementioned studies exploiting discrete photon energies along with the sublimation temperatures and unique shifts in m/z upon partial deuteration reveal the formation of at least **1b**, **2a**, and **3** (Fig. 3, 4 and 9); no evidence of isomer **4** could be provided. At photon energies of 9.20 eV, enols were detected, whose identity is deciphered in the sections below.

3.2.2 Higher dose experiments. As discussed above, isomer **4** was not formed in the experiments, therefore, its tautomer, **9**, does not have to be considered since it requires **4** as a precursor. Considering the computed adiabatic IEs of the enols, five photon energies of 9.20, 8.64, 8.25, 7.96, and 7.60 eV were selected (Fig. 3). *First*, photons with an energy of 9.20 eV can ionize *all* enols since this photon energy is above the IE of each enol isomer (**5** (IE = 7.70–7.90 eV)), **6** (IE = 8.75–8.95 eV), **7** (IE = 8.02–8.47 eV), **8** (IE = 8.46–8.94 eV). Enols **5** and **6**, **7**, **8** are the second-generation products that can be formed *via* keto-enol tautomerization of the primary products **1**, **2**, and **3**, respectively (Fig. 2a). *Second*, 8.64 eV photons can ionize only **5**, **7**, and **8c** but not **8a**–**8b** and **6**. *Third*, the 8.25 eV photons can only ionize **5** and **7a**; 7.96 eV photons can only ionize **5**. *Finally*, at a photon energy of 7.60 eV, no isomer can be ionized. Therefore, by comparing the TPD profiles of the ions at m/z = 74 at these distinct photon energies, evidence for the identification of enols can be obtained. Fig. 8 compiles the PI-ReTOF-MS data of the desorbed molecules from the irradiated CH_3OH–CH_3CHO ices. Fig. 8 is required to extract TPD profiles of m/z = 74 ($C_3H_6O_2^+$) at five photon energies (Fig. 10a–e).

At a photon energy of 9.20 eV, both TPD traces at m/z = 74 for the low-dose and higher dose irradiation in the CH_3OH–CH_3CHO ice reveal a broad signal from 150 K to 260 K (Fig. 10a). This broad sublimation event can be associated with *any* enol (IE = 7.70–8.95 eV). Lowering the photon energy to 8.64 eV, the TPD profile at m/z = 74 differs significantly from that of 9.20 eV. Three sublimation events peaking at 200 K, 219 K, and 235 K are evident (Fig. 10b). Since 8.64 eV photons cannot ionize **8a**, **8b**, and **6** (IE = 8.67–8.95 eV), these three sublimation events are associated with **5**, **7**, and/or **8c** (IE = 7.70–8.62 eV). By comparing the TPD profiles at 9.20 eV and 8.64 eV, their difference in TPD profiles (Fig. 10b, inset) must result from the presence of **8a**, **8b**, and/or **6**. After tuning the photon energy to 8.25 eV, only two sublimation events peaking at 200 K and 219 K are present (Fig. 10c). At 8.25 eV, **5** and/or **7a** can be ionized. Similarly, compared with the TPD profile collected at 8.64 eV, the difference in TPD profiles (Fig. 10c, inset) shows the sublimation event at 235 K is eliminated at 8.25 eV. Therefore, the 'missing' sublimation event is associated with **7b** and/or **8c** (IE = 8.31–8.62 eV). Since only **5** and **7a** (IE = 7.70–8.18 eV) can be ionized at 8.25 eV (Fig. 3), these two sublimation events peaking at 200 K and 219 K are associated with **5** and/or **7a**. To further identify **5** (IE = 7.70–7.90 eV) and **7a** (IE = 8.02–8.18 eV), we then lowered the photon energy to 7.96 eV, at which only **5** can be ionized. In contrast to the result at 8.25 eV, the first sublimation event at 200 K vanishes at 7.96 eV (Fig. 10d, inset), suggesting this event can only link to **7a**. The remaining sublimation event must be linked to conformer pair **5a** and/or **5b**. Further lowering the photon energy to 7.60 eV eliminates the second sublimation peak at 219 K and no other sublimation events were observed (Fig. 10e).

Recall that at 9.20 eV for the low-dose experiment, the TPD profile at m/z = 76 in the irradiated CH_3OH–CD_3CHO ice, a signal remains from 160 to 250 K (Fig. 9b), which is linked to enols. Since the ion signals at m/z = 76 can only result from **3**, therefore, the possible enol that contributes to the remaining signal at 9.20 eV is its tautomer, **8** (Fig. 2a). In addition, the difference in TPD profiles between 9.20 eV and 8.64 eV (Fig. 10b, inset) originates from **8a**, **8b**, and/or **6**. We then compared these TPD profiles as shown in Fig. 10f. The difference in their TPD profiles results from the presence of **6**, showing three sublimation events peaking at 185 K, 208 K, and 238 K (Fig. 10f, inset). As discussed above, the third sublimation event at 235 K collected at 8.64 eV (Fig. 10b) is associated with **7b** or **8c**. However, the sublimation event of **8** shows nearly background level signal only at 235 K (Fig. 10f), thus this sublimation peak at 235 K is linked to **7b**. Based on the identification of these distinct enols along with their sublimation profiles, the deconvolution of TPD profiles is shown in Fig. 11 and it matches well with the measured TPD profile at 9.20 eV. Overall, these investigations identified enols **5**–**8**.

4. Conclusions

To conclude, the present work provides compelling evidence on the formation of hydroxy-acetone (CH_3COCH_2OH, **1**), methyl acetate (CH_3COOCH_3, **2**), and 3-hydroxypropanal ($HCOCH_2CH_2OH$, **3**) as well as their enol tautomers (**5**–**8**) in methanol (CH_3OH)–acetaldehyde (CH_3CHO) ices at 5 K subjected to energetic electrons with radiation doses equivalent to a few million years of exposure to GCRs inside a prototype molecular cloud.[66]

These molecules were identified during the sublimation phase utilizing isomer-selective photoionization reflectron time-of-flight mass spectrometry (PI-ReTOF-MS) along with isotopic labeling experiments. Among these molecules, only **1** and **2** have been detected in the ISM.[25,26] Employing ice mixtures composed of the first detected six-atom molecule (methanol) and the first detected seven-atom molecule (acetaldehyde) in ISM, our results provide detailed insights into the formation mechanism of distinct $C_3H_6O_2$ isomers. *First*, the low-dose irradiation in CH_3OH–CH_3CHO ices results in the formation of **1b**, **2a**, and **3** *via* radical–radical recombination reactions. Although the atomic hydrogen loss of acetaldehyde can produce the acetyl ($CH_3\dot{C}O$) *and* the vinoxy radical ($\dot{C}H_2CHO$),[36] the acetyl radical ($CH_3\dot{C}O$) represents the dominant product.[89] This is confirmed by our FTIR results, in which only acetyl radical ($CH_3\dot{C}O$) is observed in the irradiated ice at 5 K with the vinoxy radical ($\dot{C}H_2CHO$) at the detection limit. Greeley *et al.* and Bennett *et al.* suggested that the decomposition of methanol to the hydroxymethyl radical ($\dot{C}H_2OH$) *via* C–H scission exceeds the formation of the methoxy radical ($CH_3\dot{O}$) *via* CH_3O–H scission due to distinct reaction endoergicities of 389 and 421 kJ mol^{-1}, respectively (reactions (9) and (10)).[40,90,91] Consequently, the yield of **4** formed *via* recombination between methoxy radical ($CH_3\dot{O}$) and the vinoxy radical ($\dot{C}H_2CHO$) (reaction (8)) is expected to be small. This is documented in the absence of **4** in our experiments. On the other hand, isomers **1–3** can be formed easily *via* reactions (3), (5), and (7). Note that the overall reaction energies to yield **1–3** from methanol and acetaldehyde (reactions (11)–(13)) are +422, +383 and +451 kJ mol^{-1}, respectively, with the endoergicity compensated by the kinetic energy of the impinging electrons. Therefore, these data alone demonstrate the necessity of non-equilibrium chemistry in the formation of the aforementioned isomers. *Second*, enols **5–8** are formed by exposing CH_3OH–CH_3CHO ices to energetic electrons *via* keto–enol tautomerization of the primary products (Fig. 12).

$$CH_3OH \rightarrow \dot{C}H_2OH + H \quad (9)$$

$$CH_3OH \rightarrow CH_3\dot{O} + H \quad (10)$$

$$CH_3OH + CH_3CHO \rightarrow CH_3COCH_2OH + 2H \quad (11)$$

$$CH_3OH + CH_3CHO \rightarrow CH_3COOCH_3 + 2H \quad (12)$$

$$CH_3OH + CH_3CHO \rightarrow HCOCH_2CH_2OH + 2H \quad (13)$$

Few studies have been reported on enols **5–8** in the literature. Hydroxyacetone (**1**) can form **5** (prop-1-ene-1,2-diol) and **6** (prop-2-ene-1,2-diol) *via* tautomerization.[55,92,93] **5** was reported to be one of the top 100 most abundant chemical constituents in the mainstream aerosol of the Tobacco Heating System 2.2.[94] Using diffuse reflectance infrared Fourier transform (DRIFT) spectroscopy, Vila *et al.* reported the bands attributed to the C=C bond vibration of **5** and **6** in the reduced copper catalyst to be at around 1670 cm^{-1} and 1631 cm^{-1}, respectively.[59] The absence of these two band positions in our FTIR data is probably due to their weak signals. Based on the ^{1}H NMR data, they found

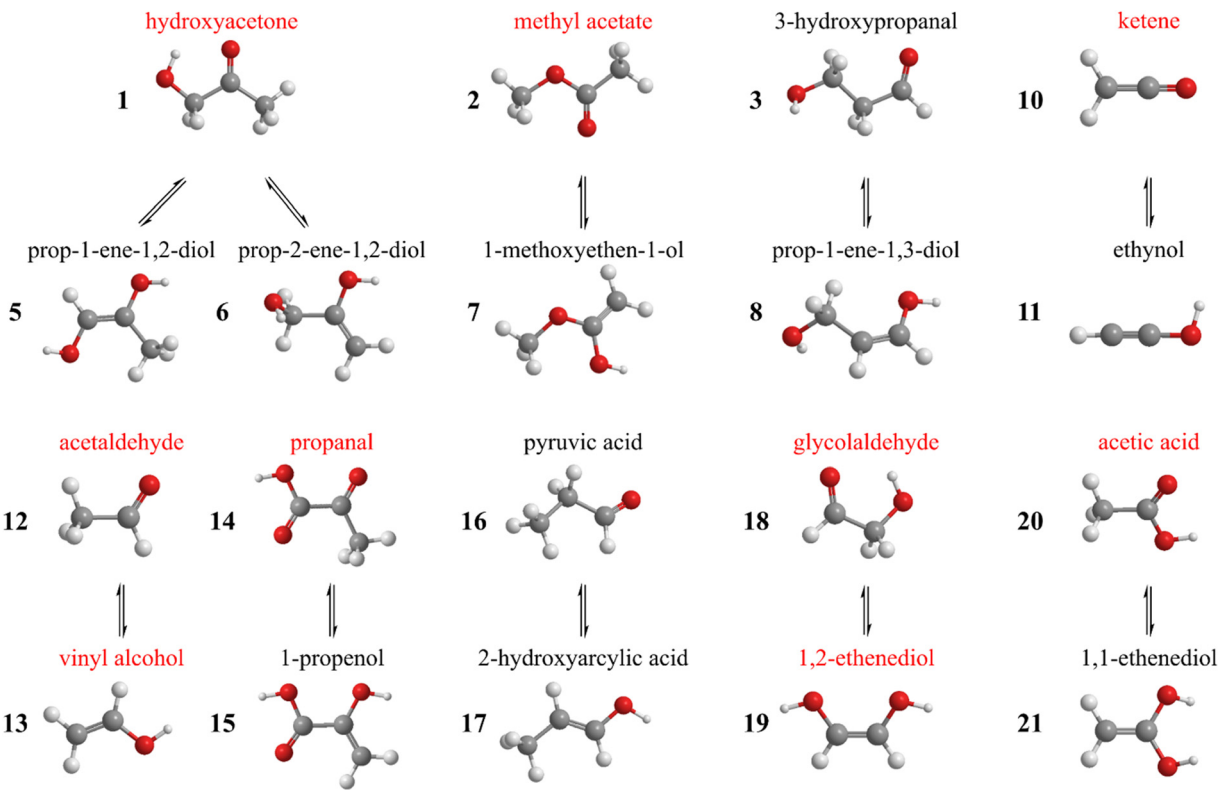

Fig. 12 Enol tautomer pairs detected in different interstellar analog ices in our laboratory. Isomers color-coded in red indicate astronomical detections.

that **6** is the most favorable isomer for producing 1,2-propanediol ($CH_3CH(OH)CH_2OH$) *via* direct reduction.[59] In addition, **6** can be formed *via* the dehydration of glycerol,[58,59] a key molecule pertaining to the origins of life, which can be formed in irradiated CH_3OH ice.[11]

The tautomerization of methyl acetate (**2**) was speculated to lead to **7** (1-methoxyethen-1-ol) *via* a four-membered cyclic transition state.[95] Guthrie *et al.* calculated the free energy for the formation of **7** to be -219.6 ± 6.4 kJ mol^{-1}.[96] Besides, enol **7** can be formed in the concerted process of the thermolysis reaction of methyl-3-hydroxypropanoate *via* a six-membered cyclic transition state.[97] The keto-enol tautomerism of 3-hydroxypropanal (**3**) can lead to the formation of enol **8** (prop-1-ene-1,3-diol).[98] Kirkok *et al.* suggested that **8** can be converted to acrolein (CH_2CHCHO) *via* dehydration reaction at a significantly low enthalpy change of 63 kJ mol^{-1}.[99] To the best of our knowledge, enols **7** and **8** have not been detected experimentally in the literature.

Simple enols are typically thought to be short-lived species in preparative organic synthesis;[64] however, they may have a long lifetime in the ISM environment because they cannot overcome tautomerization barriers at the low temperatures and pressures in the gas phase.[16] In our experiments, considering the distance between the wafer surface and the photoionization region of 2.0 ± 0.5 mm[100] along with the average velocity of 239 m s^{-1} for the enols subliming at an average temperature of 200 K, the lifetime of the enols has to exceed 8.4 ± 2.1 μs. Fig. 12 depicts the enol tautomer pairs detected after the processing of interstellar analog ices in our laboratory. Though only two enols (vinyl alcohol (C_2H_3OH) and 1,2-ethenediol (HOCHCHOH)) have been detected yet in deep space,[62,63] it was suggested that enols should be ubiquitous in the interstellar medium.[16,45,61] Interestingly, Kleimeier *et al.* (2021) reported the identification of 1,2-ethenediol in low-temperature methanol-bearing ices at 5 K,[45] the same molecule was detected very recently by Rivilla *et al.* (2022) in the interstellar medium toward the G + 0.693–0.027 molecular cloud.[63] It should be noted that our laboratory experiments revealed that the hitherto astronomically unobserved isomers 3-hydroxypropanal ($HCOCH_2CH_2OH$, **3**) and enols (**5–8**) could be generated within interstellar ices from methanol-rich and acetaldehyde-rich star-forming regions. Once these molecules are formed, they can subsequently be released into the gas phase in the hot core stage. Thus, these molecules represent promising candidates for future astronomical searches *via* radio telescopes such as the Atacama Large Millimeter/submillimeter Array (ALMA). Due to their nucleophilic character and high reactivity,[61] those enols as reactive intermediates may be of particular importance to our understanding of the molecular synthesis of biologically relevant molecules in deep space.[45] It should be stressed that no simulation experiment can replicate the chemical complexity of the interstellar medium, however, simulation experiments conducted with well-defined model ices as presented here help understand the reaction pathways leading to key organics such as enols in the ices.[45] Future experiments incorporating molecules such as water into the mixture ice may unravel the formation mechanisms of other COMs in deep space.

The results presented here demonstrate that PI-ReTOF-MS offers a powerful methodology to discriminate between isomers of COMs including biorelevant molecules formed in interstellar analog ices upon interaction with ionizing radiation.[2,11] Tunable VUV light (7–11 eV) is necessary for the soft photoionization process since the relevant $C_3H_6O_2$ isomers present in this work have ionization energies between 7.70 and 10.40 eV. By using tunable single-photon ionization, the complete product spectrum based on distinct mass-to-charge ratios of the ionized molecules can be measured during the TPD phase. Utilizing isotopic substitution experiments along with temperature-programmed desorption, the formation pathways of isomers **1–3**, as well as their enol tautomers **5–8**, were identified. Though FTIR spectroscopy allows the functional groups of COMs to be detected within the astrophysical ice analogs, it does not always identify individual molecules due to the similar functional groups and subsequent overlapping frequen-cies.[42,67] For instance, carbonyls like aldehydes and ketones represent similar group frequencies in the range of 1850 cm^{-1} to 1600 cm^{-1}.[67,101] The absence of absorption positions in our FTIR data for the $C_3H_6O_2$ isomers detected in the present work (Fig. 12) suggests that PI-ReTOF-MS provides higher sensitivity to the identification of $C_3H_6O_2$ isomers in interstellar analog ices.

Conflicts of interest

The authors declare no competing financial interests.

Acknowledgements

The experimental work was supported by the US National Science Foundation, Division of Astronomical Sciences under grants AST-2103269 awarded to the University of Hawaii at Manoa. *Ab initio* calculations at Lebedev Physics Institute were supported by the Ministry of Science and Higher Education of the Russian Federation under Grant No. 075-15-2021-597.

References

1 E. Herbst and E. F. V. Dishoeck, *Annu. Rev. Astron. Astrophys.*, 2009, **47**, 427–480.
2 A. M. Turner and R. I. Kaiser, *Acc. Chem. Res.*, 2020, **53**, 2791–2805.
3 G. M. Muñoz Caro, U. J. Meierhenrich, W. A. Schutte, B. Barbier, A. Arcones Segovia, H. Rosenbauer, W. H. P. Thiemann, A. Brack and J. M. Greenberg, *Nature*, 2002, **416**, 403–406.
4 P. D. Holtom, C. J. Bennett, Y. Osamura, N. J. Mason and R. I. Kaiser, *Astrophys. J.*, 2005, **626**, 940–952.
5 M. Nuevo, Y. J. Chen, T. S. Yih, W. H. Ip, H. S. Fung, C. Y. Cheng, H. R. Tsai and C. Y. R. Wu, *Adv. Space Res.*, 2007, **40**, 1628–1633.
6 M. Nuevo, G. Auger, D. Blanot and L. d'Hendecourt, *Orig. Life Evol. Biosph.*, 2008, **38**, 37–56.

7 P. de Marcellus, C. Meinert, M. Nuevo, J.-J. Filippi, G. Danger, D. Deboffle, L. Nahon, L. Le Sergeant d'Hendecourt and U. J. Meierhenrich, *Astrophys. J.*, 2011, **727**, L27.
8 R. I. Kaiser, A. M. Stockton, Y. S. Kim, E. C. Jensen and R. A. Mathies, *Astrophys. J.*, 2013, **765**, 111.
9 M. P. Bernstein, S. A. Sandford, L. J. Allamandola, J. S. Gillette, S. J. Clemett and R. N. Zare, *Science*, 1999, **283**, 1135–1138.
10 C. J. Bennett, Y. Osamura, M. D. Lebar and R. I. Kaiser, *Astrophys. J.*, 2005, **634**, 698–711.
11 R. I. Kaiser, S. Maity and B. M. Jones, *Angew. Chem., Int. Ed.*, 2015, **54**, 195–200.
12 A. Bergantini, P. Maksyutenko and R. I. Kaiser, *Astrophys. J.*, 2017, **841**, 96.
13 G. Fedoseev, K. J. Chuang, S. Ioppolo, D. Qasim, E. F. V. Dishoeck and H. Linnartz, *Astrophys. J.*, 2017, **842**, 52.
14 A. Bergantini, S. Góbi, M. J. Abplanalp and R. I. Kaiser, *Astrophys. J.*, 2018, **852**, 70.
15 C. Zhu, R. Frigge, A. Bergantini, R. C. Fortenberry and R. I. Kaiser, *Astrophys. J.*, 2019, **881**, 156.
16 N. F. Kleimeier and R. I. Kaiser, *ChemPhysChem*, 2021, **22**, 1229–1236.
17 C. Zhu, A. M. Turner, M. J. Abplanalp, R. I. Kaiser, B. Webb, G. Siuzdak and R. C. Fortenberry, *Astrophys. J.*, 2020, **899**, L3.
18 K. Plankensteiner, H. Reiner and B. M. Rode, *Curr. Org. Chem.*, 2005, **9**, 1107–1114.
19 N. Kitadai and S. Maruyama, *Geosci. Front.*, 2018, **9**, 1117–1153.
20 M. J. Abplanalp, S. Gozem, A. I. Krylov, C. N. Shingledecker, E. Herbst and R. I. Kaiser, *Proc. Natl. Acad. Sci. U. S. A.*, 2016, **113**, 7727–7732.
21 S. Petrie, *Astrophys. J. Lett.*, 1995, **454**, L165.
22 R. I. Kaiser, *Chem. Rev.*, 2002, **102**, 1309–1358.
23 R. Garrod, I. Hee Park, P. Caselli and E. Herbst, *Faraday Discuss.*, 2006, **133**, 51–62.
24 E. Herbst, *Front. Astron. Space Sci.*, 2021, **8**, 207.
25 Y. Zhou, D.-H. Quan, X. Zhang and S.-L. Qin, *Res. Astron. Astrophys.*, 2020, **20**, 125.
26 B. Tercero, I. Kleiner, J. Cernicharo, H. V. L. Nguyen, A. López and G. M. M. Caro, *Astrophys. J.*, 2013, **770**, L13.
27 M. Tudorie, I. Kleiner, J. T. Hougen, S. Melandri, L. W. Sutikdja and W. Stahl, *J. Mol. Spectrosc.*, 2011, **269**, 211–225.
28 A. J. Apponi, J. J. Hoy, D. T. Halfen, L. M. Ziurys and M. A. Brewster, *Astrophys. J.*, 2006, **652**, 1787–1795.
29 R. Braakman, B. J. Drouin, S. L. Widicus Weaver and G. A. Blake, *J. Mol. Spectrosc.*, 2010, **264**, 43–49.
30 J.-B. Bossa, M. H. Ordu, H. S. P. Müller, F. Lewen and S. Schlemmer, *Astron. Astrophys.*, 2014, **570**, A12.
31 P. R. Story and J. R. Burgess, *J. Am. Chem. Soc.*, 1967, **89**, 5726–5727.
32 T. Leonardo, L. Baptista, E. C. da Silva and G. Arbilla, *J. Phys. Chem. A*, 2011, **115**, 7709–7721.
33 A. Das, L. Majumdar, D. Sahu, P. Gorai, B. Sivaraman and S. K. Chakrabarti, *Astrophys. J., Lett.*, 2015, **808**, 21.
34 B. Sivaraman, R. Mukherjee, K. P. Subramanian and S. B. Banerjee, *Chem. Phys. Lett.*, 2014, **609**, 167–171.
35 R. T. Garrod, S. L. W. Weaver and E. Herbst, *Astrophys. J.*, 2008, **682**, 283–302.
36 N. F. Kleimeier, A. K. Eckhardt and R. I. Kaiser, *Astrophys. J.*, 2020, **901**, 84.
37 N. F. Kleimeier, A. K. Eckhardt, P. R. Schreiner and R. I. Kaiser, *Chem*, 2020, **6**, 3385–3395.
38 N. F. Kleimeier, M. J. Abplanalp, R. N. Johnson, S. Gozem, J. Wandishin, C. N. Shingledecker and R. I. Kaiser, *Astrophys. J.*, 2021, **911**, 24.
39 A. M. Turner, A. Bergantini, A. S. Koutsogiannis, N. F. Kleimeier, S. K. Singh, C. Zhu, A. K. Eckhardt and R. I. Kaiser, *Astrophys. J.*, 2021, **916**, 74.
40 C. J. Bennett, S. H. Chen, B. J. Sun, A. H. H. Chang and R. I. Kaiser, *Astrophys. J.*, 2007, **660**, 1588–1608.
41 S. Maity, R. I. Kaiser and B. M. Jones, *Faraday Discuss.*, 2014, **168**, 485.
42 S. Maity, R. I. Kaiser and B. M. Jones, *Phys. Chem. Chem. Phys.*, 2015, **17**, 3081–3114.
43 S. Góbi, P. B. Crandall, P. Maksyutenko, M. Förstel and R. I. Kaiser, *J. Phys. Chem. A*, 2018, **122**, 2329–2343.
44 C. Zhu, A. M. Turner, C. Meinert and R. I. Kaiser, *Astrophys. J.*, 2020, **889**, 134.
45 N. F. Kleimeier, A. K. Eckhardt and R. I. Kaiser, *J. Am. Chem. Soc.*, 2021, **143**, 14009–14018.
46 C. Zhu, N. F. Kleimeier, A. M. Turner, S. K. Singh, R. C. Fortenberry and R. I. Kaiser, *Proc. Natl. Acad. Sci. U. S. A.*, 2022, **119**, e2111938119.
47 N. F. Kleimeier, A. M. Turner, R. C. Fortenberry and R. I. Kaiser, *ChemPhysChem*, 2020, **21**, 1531–1540.
48 H. E. Matthews, P. Friberg and W. M. Irvine, *Astrophys. J.*, 1985, **290**, 609–614.
49 M. Ikeda, M. Ohishi, A. Nummelin, J. E. Dickens, P. Bergman, A. Hjalmarson and W. M. Irvine, *Astrophys. J.*, 2001, **560**, 792–805.
50 G. J. White, M. Araki, J. S. Greaves, M. Ohishi and N. S. Higginbottom, *Astron. Astrophys.*, 2003, **407**, 589–607.
51 A. Fuente, J. Cernicharo, P. Caselli, C. McCoey, D. Johnstone, M. Fich, T. van Kempen, A. Palau, U. A. Yıldız, B. Tercero and A. López, *Astron. Astrophys.*, 2014, **568**, A65.
52 B. Parise, C. Ceccarelli, A. G. G. M. Tielens, E. Herbst, B. Lefloch, E. Caux, A. Castets, I. Mukhopadhyay, L. Pagani and L. Loinard, *Astron. Astrophys.*, 2002, **393**, L49–L53.
53 S. Cazaux, A. G. G. M. Tielens, C. Ceccarelli, A. Castets, V. Wakelam, E. Caux, B. Parise and D. Teyssier, *Astrophys. J.*, 2003, **593**, L51–L55.
54 E. L. Gibb, D. C. B. Whittet, A. C. A. Boogert and A. G. G. M. Tielens, *Astrophys. J., Suppl. Ser.*, 2004, **151**, 35–73.
55 V. A. Yaylayan, S. Harty-Majors and A. A. Ismail, *J. Agric. Food Chem.*, 1999, **47**, 2335–2340.
56 M. D. Topal and J. R. Fresco, *Nature*, 1976, **263**, 285–289.
57 O. Tapia, J. Andres and V. S. Safont, *J. Phys. Chem.*, 1994, **98**, 4821–4830.
58 S.-H. Chai, H.-P. Wang, Y. Liang and B.-Q. Xu, *Green Chem.*, 2007, **9**, 1130–1136.

59 F. Vila, M. López Granados and R. Mariscal, *Catal. Sci. Technol.*, 2017, **7**, 3119–3127.
60 A. M. Turner, A. S. Koutsogiannis, N. F. Kleimeier, A. Bergantini, C. Zhu, R. C. Fortenberry and R. I. Kaiser, *Astrophys. J.*, 2020, **896**, 88.
61 N. F. Kleimeier and R. I. Kaiser, *J. Phys. Chem. Lett.*, 2022, **13**, 229–235.
62 B. E. Turner and A. J. Apponi, *Astrophys. J.*, 2001, **561**, L207–L210.
63 V. M. Rivilla, L. Colzi, I. Jiménez-Serra, J. Martín-Pintado, A. Megías, M. Melosso, L. Bizzocchi, Á. López-Gallifa, A. Martínez-Henares, S. Massalkhi, B. Tercero, P. de Vicente, J.-C. Guillemin, J. García de la Concepción, F. Rico-Villas, S. Zeng, S. Martín, M. A. Requena-Torres, F. Tonolo, S. Alessandrini, L. Dore, V. Barone and C. Puzzarini, *Astrophys. J. Lett.*, 2022, **929**, L11.
64 H. Hart, *Chem. Rev.*, 1979, **79**, 515–528.
65 M. Oliva, V. S. Safont, J. Andrés and O. Tapia, *J. Phys. Chem. A*, 1999, **103**, 6009–6016.
66 A. G. Yeghikyan, *Astrophysics*, 2011, **54**, 87–99.
67 M. J. Abplanalp, M. Forstel and R. I. Kaiser, *Chem. Phys. Lett.*, 2016, **644**, 79–98.
68 C. Zhu, A. Bergantini, S. K. Singh, R. I. Kaiser, A. K. Eckhardt, P. R. Schreiner, Y.-S. Huang, B.-J. Sun and A. H. H. Chang, *Chem. Commun.*, 2021, **57**, 4958–4961.
69 Z. Dai, S. Gao, J. Wang and Y. Mo, *J. Chem. Phys.*, 2014, **141**, 144306.
70 A. Bergantini, M. J. Abplanalp, P. Pokhilko, A. I. Krylov, C. N. Shingledecker, E. Herbst and R. I. Kaiser, *Astrophys. J.*, 2018, **860**, 108.
71 B. M. Jones and R. I. Kaiser, *J. Phys. Chem. Lett.*, 2013, **4**, 1965–1971.
72 A. M. Turner, M. J. Abplanalp, S. Y. Chen, Y. T. Chen, A. H. Chang and R. I. Kaiser, *Phys. Chem. Chem. Phys.*, 2015, **17**, 27281–27291.
73 M. Bouilloud, N. Fray, Y. Bénilan, H. Cottin, M.-C. Gazeau and A. Jolly, *Mon. Not. R. Astron. Soc.*, 2015, **451**, 2145–2160.
74 R. L. Hudson and F. M. Coleman, *Phys. Chem. Chem. Phys.*, 2019, **21**, 11284–11289.
75 R. L. Hudson, M. J. Loeffler, R. F. Ferrante, P. A. Gerakines and F. M. Coleman, *Astrophys. J.*, 2020, **891**, 22.
76 D. M. Hudgins, S. A. Sandford, L. J. Allamandola and A. G. Tielens, *Astrophys. J., Suppl. Ser.*, 1993, **86**, 713–870.
77 D. Drouin, A. R. Couture, D. Joly, X. Tastet, V. Aimez and R. Gauvin, *Scanning*, 2007, **29**, 92–101.
78 R. Hilbig and R. Wallenstein, *IEEE J. Quantum Electron.*, 1983, **19**, 194–201.
79 J.-D. Chai and M. Head-Gordon, *Phys. Chem. Chem. Phys.*, 2008, **10**, 6615–6620.
80 J. Dunning and H. Thom, *J. Chem. Phys.*, 1989, **90**, 1007–1023.
81 T. B. Adler, G. Knizia and H.-J. Werner, *J. Chem. Phys.*, 2007, **127**, 221106.
82 G. Knizia, T. B. Adler and H.-J. Werner, *J. Chem. Phys.*, 2009, **130**, 054104.
83 J. Zhang and E. F. Valeev, *J. Chem. Theory Comput.*, 2012, **8**, 3175–3186.
84 M. Frisch, G. Trucks, H. Schlegel, G. Scuseria, M. Robb, J. Cheeseman, G. Scalmani, V. Barone, B. Mennucci and G. Petersson, *et al.*, *Gaussian 16, Revision C.1*, Gaussian Inc., Wallingford CT, 2019.
85 H.-J. Werner, P. Knowles, R. Lindh, F. R. Manby, M. Schütz, P. Celani, T. Korona, G. Rauhut, R. Amos and A. Bernhardsson, *et al.*, MOLPRO, Version 2021.2, A package of ab initio programs; University of Cardiff, Cardiff, U.K., 2021, see http://www.molpro.net.
86 M. E. Jacox, *Chem. Phys.*, 1982, **69**, 407–422.
87 O. Kostko, B. Bandyopadhyay and M. Ahmed, *Annu. Rev. Phys. Chem.*, 2016, **67**, 19–40.
88 M. J. Abplanalp and R. I. Kaiser, *Phys. Chem. Chem. Phys.*, 2019, **21**, 16949–16980.
89 D. Mei, A. M. Karim and Y. Wang, *ACS Catal.*, 2012, **2**, 468–478.
90 J. Greeley and M. Mavrikakis, *J. Am. Chem. Soc.*, 2004, **126**, 3910–3919.
91 A. H. H. Chang and S. H. Lin, *Chem. Phys. Lett.*, 2004, **384**, 229–235.
92 S. Najmi, J. So, E. Stavitski, W. P. McDermott, Y. Lyu, S. P. Burt, I. Hermans, D. S. Sholl and C. Sievers, *ChemCatChem*, 2021, **13**, 445–458.
93 J. E. De Vrieze, J. W. Thybaut and M. Saeys, *ACS Catal.*, 2019, **9**, 3831–3839.
94 M. C. Bentley, M. Almstetter, D. Arndt, A. Knorr, E. Martin, P. Pospisil and S. Maeder, *Anal. Bioanal. Chem.*, 2020, **412**, 2675–2685.
95 E. Zapata, J. Gaviria and J. Quijano, *Int. J. Chem. Kinet.*, 2007, **39**, 92–96.
96 J. P. Guthrie and Z. Liu, *Can. J. Chem.*, 1995, **73**, 1395–1398.
97 D. Rodríguez-Linares, E. Codorniu-Hernández, E. Velez-Ortíz, J.-A. Murillo-López, P.-A. Villegas-Bolaños and J. Quijano-Tobón, *J. Mol. Struct.: THEOCHEM*, 2009, **902**, 41–48.
98 P. E. A. Debiagi, G. Gentile, M. Pelucchi, A. Frassoldati, A. Cuoci, T. Faravelli and E. Ranzi, *Biomass Bioenergy*, 2016, **93**, 60–71.
99 S. K. Kirkok, J. K. Kibet, F. Okanga, T. Kinyanjui and V. Nyamori, *BMC Chem.*, 2019, **13**, 126.
100 C. Zhang, C. Zhu, A. K. Eckhardt and R. I. Kaiser, *J. Phys. Chem. Lett.*, 2022, **13**, 2725–2730.
101 G. Socrates, *Infrared and Raman Characteristic Group Frequencies*, John Wiley & Sons, Ltd., New York, 3rd edn, 2004.
102 H. Hollenstein and H. H. Günthard, *Spectrochim. Acta, Part A*, 1971, **27**, 2027–2060.
103 M. Falk and E. Whalley, *J. Chem. Phys.*, 1961, **34**, 1554–1568.